Evaluation of NorESM-OC (versions 1 and 1.2), the ocean carbon-cycle stand-alone configuration of the Norwegian Earth System Model (NorESM1)

J. Schwinger[1], N. Goris[1], J. Tjiputra[1], I. Kriest[2], M. Bentsen[1], I. Bethke[1], M. Ilicak[1], K. Assmann[3,a], and C. Heinze[3,1]

[1]Uni Research Climate, Bjerknes Centre for Climate Research, Bergen, Norway
[2]GEOMAR Helmholtz-Zentrum für Ozeanforschung, Kiel, Germany
[3]Geophysical Institute, University of Bergen, Bjerknes Centre for Climate Research, Bergen, Norway
[a]now at: Department of Marine Sciences, University of Gothenburg, Gothenburg, Sweden

Received: 24 November 2015 – Accepted: 11 December 2015 – Published: 15 January 2016

Correspondence to: J. Schwinger (jorg.schwinger@uni.no)

Published by Copernicus Publications on behalf of the European Geosciences Union.

GMDD

doi:10.5194/gmd-2015-256

NorESM-OC

J. Schwinger et al.

GMDD

doi:10.5194/gmd-2015-256

NorESM-OC

J. Schwinger et al.

Abstract

Idealised and hindcast simulations performed with the stand-alone ocean carbon-cycle configuration of the Norwegian Earth System Model (NorESM-OC) are described and evaluated. We present simulation results of two different model versions at different grid resolutions and using two different atmospheric forcing data sets. Model version NorESM-OC1 corresponds to the version that is included in the fully coupled model NorESM-ME1, which participated in CMIP5. The main update between NorESM-OC1 and NorESM-OC1.2 is the addition of two new options for the treatment of sinking particles. We find that using a constant sinking speed, which has been the standard in NorESM's ocean carbon cycle module HAMOCC (HAMburg Ocean Carbon Cycle model) does not transport enough particulate organic carbon (POC) into the deep ocean below approximately 2000 m depth. The two newly implemented parameterisations, a particle aggregation scheme with prognostic sinking speed, and a simpler scheme prescribing a linear increase of sinking speed with depth, provide better agreement with observed POC fluxes. Additionally, reduced deep ocean biases of oxygen and remineralised phosphate indicate a better performance of the new parameterisations. For model version 1.2, a re-tuning of the ecosystem parameterisation has been performed, which (i) reduces previously too high primary production in high latitudes, (ii) consequently improves model results for surface nutrients, and (iii) reduces alkalinity and dissolved inorganic carbon biases at low latitudes. We use hindcast simulations with prescribed observed and constant (pre-industrial) atmospheric CO_2 concentrations to derive the past and contemporary ocean carbon sink. For the period 1990–1999 we find an average ocean carbon uptake ranging from 2.01 to 2.58 Pg C yr^{-1} depending on model version, grid resolution and atmospheric forcing data set.

1 Introduction

Earth system models (ESMs) have been developed to take into account feedbacks between the physical climate and biogeochemical processes in projections of climate change (Bretherton, 1985; Flato, 2011). However, due to the complexity of feedback processes, it can prove useful to run one or several submodels of an ESM independently by using prescribed data at the boundary between submodel domains, e.g. by using prescribed atmospheric conditions at the air–sea boundary to force the ocean and ice models of an ESM. Such "stand-alone" model configurations are useful to conduct idealised experiments, to perform hindcast simulations in which boundary conditions reflect the observed variability and trends, or to save computer time in cases where certain feedbacks are not expected to be important.

Here, we describe and evaluate the stand-alone ocean carbon-cycle configuration of the Norwegian Earth System Model (NorESM-OC). The Norwegian Earth System Model version 1 (NorESM1, Bentsen et al., 2013; Tjiputra et al., 2013) is derived from the Community Earth System Model (CESM, Gent et al., 2011; Lindsay et al., 2014), using the same sea-ice and land models as well as the same coupler, but a modified atmospheric model (CAM-Oslo, Kirkevåg et al., 2013), and a different ocean model. NorESM's physical ocean component originates from the Miami Isopycnic Coordinate Ocean Model (MICOM; Bleck and Smith, 1990; Bleck et al., 1992) but has been updated with modified numerics and physics as described in Bentsen et al. (2013). This model has been extended by Assmann et al. (2010) to include the HAMburg Ocean Carbon Cycle model (HAMOCC, Maier-Reimer, 1993; Maier-Reimer et al., 2005). In the NorESM-OC configuration MICOM-HAMOCC is coupled to CESM's sea-ice model CICE4 (Holland et al., 2012) and a "data atmosphere" which provides atmospheric forcing fields to the ocean and sea-ice components.

The NorESM-OC model configuration allows to study the ocean carbon cycle and related biogeochemical cycles (phosphorus, nitrogen, silicate, iron, and oxygen) in idealised or hindcast simulations. We persue two main objectives with this setup. First,

GMDD

doi:10.5194/gmd-2015-256

NorESM-OC

J. Schwinger et al.

Title Page

Abstract · Introduction

Conclusions · References

Tables · Figures

|◄ · ►|

◄ · ►

Back · Close

it provides a simplified and computationally (relatively) inexpensive framework for the implementation and testing of new or updated model parametrisations. For example, we present the implementation and evaluation of new parameterisations for the sinking of particulate organic carbon (POC) in this work. In a fully coupled model setup atmospheric CO_2 concentration is sensitive to the parameterisation of the biological pump (e.g. Marinov et al., 2006; Kwon et al., 2009), and eventually we aim to evaluate this sensitivity and associated feedbacks in the fully coupled version of NorESM. It is convenient, however, to perform a first evaluation without any feedback between biogeochemistry and physical climate (i.e., ocean circulation is unchanged in all test cases).

Second, hindcast simulations can provide insight into the response of biogeochemical cycles to observed variability and trends in atmospheric forcing. Of particular interest is the estimation of past and contemporary anthropogenic carbon uptake by the oceans using meteorological reanalysis data to force the ocean model. Such information is needed to better constrain the Earth system's contemporary carbon budget, an effort undertaken by e.g. the Global Carbon Project (GCP, Le Quéré et al., 2015). Hindcast simulations performed with a first version of this model configuration (NorESM-OC1) contributed to the annual update of this carbon budget for the years 2011 to 2013. NorESM-OC1 corresponds to the version of the fully coupled NorESM1-ME that is described in Tjiputra et al. (2013), and that participated in the phase 5 of the Coupled Model Intercomparison Project (CMIP5, Taylor et al., 2012).

In this manuscript we describe NorESM-OC1 next to an updated version of the model system (NorESM-OC1.2), which is configured on a numerically more efficient grid in 1° and 2° resolution, includes additional parameterisations for the sinking of POC, and features several updates and improvements as described in Sect. 2. Spin-up followed by hindcast simulations forced by two slightly different forcing data sets have been performed for the different model versions and configurations. We evaluate the model results against available observation based climatologies (Sects. 3.1 to 3.3), and we calculate ocean carbon sink estimates and anthropogenic carbon storage (Sect. 3.4). The

GMDD

doi:10.5194/gmd-2015-256

NorESM-OC

J. Schwinger et al.

newly implemented particle sinking schemes are evaluated using observation based estimates of global POC fluxes and of remineralisation as well as sediment trap data (Sect. 3.5). We conclude by discussing the current status of the model system and lines of further development.

2   Model description and configuration

The components of NorESM discussed here have been described and evaluated in papers published previously in this special section (Bentsen et al., 2013; Tjiputra et al., 2013) and elsewhere (Danabasoglu et al., 2014; Griffies et al., 2014; Downes et al., 2015; Farneti et al., 2015). Therefore, we only give a brief description of the NorESM-OC model components and focus on documenting the specific model configurations and the updates made for NorESM-OC1.2.

2.1   The physical ocean model MICOM

The main benefit of an isopycnal model is the good control on the diapycnal mixing (less numerical diffusion across isopycnic surfaces) that helps to preserve water masses during long model integrations. As mentioned above, the model is based on MICOM as described by Bleck and Smith (1990) and Bleck et al. (1992). Key aspects retained from this model version are a mass conserving formulation (non-Boussinesq), Arakawa C-grid discretisation, leap-frog and forward-backward time stepping for the baroclinic and barotropic mode, respectively, and a potential vorticity/enstrophy conserving scheme for the momentum equation.

Different from the original MICOM, we use the incremental remapping algorithm of Dukowicz and Baumgardner (2000) for transport of layer thickness, potential temperature, salinity, and tracers. The second order accurate algorithm is expressed in flux form and thus conserves mass by construction. Furthermore, it guarantees monotonic-

GMDD

doi:10.5194/gmd-2015-256

NorESM-OC

J. Schwinger et al.

Discussion Paper | Discussion Paper | Discussion Paper | Discussion Paper

ity of tracers (i.e., the scheme does not create new minima or maxima) for any velocity field.

Originally, MICOM had a single bulk surface mixed layer while in NorESM the mixed layer is divided into two model layers with freely evolving density and equal thickness when the mixed layer is shallower than 20 m. The uppermost layer is limited to 10 m when the mixed layer is deeper than 20 m. The main reason for this is to allow for a faster ocean surface response to surface fluxes. We achieve reduced mixed layer depth biases (compared to original MICOM) by using a turbulent kinetic energy (TKE) model based on Oberhuber (1993), extended with a parametrisation of mixed layer re-stratification by submesoscale eddies (Fox-Kemper et al., 2008). To improve the representation of water masses in weakly stratified high latitude halocline, the static stability of the uppermost layers is measured by in-situ density jumps across layer interfaces, thus allowing for layers that are unstable with respect to potential density referenced at 2000 dbar to exist. The diagnostic version of the eddy closure of Eden and Greatbatch (2008) as implemented by Eden et al. (2009) is used to parameterise the thickness and isopycnal eddy diffusivity. Further, to reduce sea surface salinity and stratification biases at high latitudes, salt released during freezing of sea ice can be distributed below the mixed layer.

The ocean component exchanges no mass with the other components of NorESM. Thus, freshwater fluxes are converted to virtual salt and tracer fluxes before they are applied to the ocean.

2.2 The sea ice model CICE

NorESM-OC employs the CESM sea ice component, which is based on version 4 of the Los Alamos National Laboratory sea ice model (CICE4, Hunke and Lipscomb, 2008). Important modifications of this model that are utilised in CESM and NorESM1 are the delta-Eddington short-wave radiation transfer as well as melt pond and aerosol parameterisations, all described by Holland et al. (2012). The sea-ice model shares the same horizontal grid with the ocean component of NorESM.

Discussion Paper | Discussion Paper | Discussion Paper | Discussion Paper |

GMDD

doi:10.5194/gmd-2015-256

NorESM-OC

J. Schwinger et al.

2.3 The marine biogeochemistry model HAMOCC 5

The HAMburg Ocean Carbon Cycle (HAMOCC 5) model is based on the original work of Maier-Reimer (1993) and subsequent refinements (Maier-Reimer et al., 2005). The model simulates the marine biogeochemical cycles of carbon, nitrogen, phosphorus,

5 silicate, iron, and oxygen, including the fluxes of these elements across the air–sea interface. HAMOCC 5.1 was coupled with the isopycnic MICOM model by Assmann et al. (2010). We describe a version of the code that evolved from this point and note that the original model has also been further developed by the biogeochemistry group at Max Planck Institute in Hamburg (Ilyina et al., 2013). The HAMOCC code is em-

10 bedded in MICOM, and hence runs at the same spatial and temporal resolution as the ocean model. The model has 19 prognostic tracers (Table 1), all of which are advected and diffused with the ocean circulation provided by MICOM. Two additional tracers are needed if the particle aggregation scheme (prognostic sinking speed, see Sect. 2.3.3) is switched on. There are also three "preformed" tracers for oxygen, phosphate, and

15 alkalinity, which are set to the respective concentration values in the surface mixed layer, and are otherwise passively advected. Preformed tracers have been introduced in version 1.2 to enhance the diagnostic capabilities of the model.

When HAMOCC was implemented as the biogeochemistry module of MICOM, the biogeochemical tracers were only defined at one of the two time-levels of the leap-frog

20 time stepping scheme to increase computational efficiency (Assmann et al., 2010). Since the physical fields undergo a time-smoothing at the end of each time-step, but the biogeochemical tracers do not, there is an inconsistency between physical fields and biogeochemical tracers introduced by this simplification, which results in a non-conservation or tracer mass. This non-conservation is accounted for in model version 1

25 by a correction factor applied after the time-smoothing to the biogeochemical tracer fields. Although simulation results were not seriously affected on integration time scales of ≈ 1000 years we decided to re-implement the tracer transport fully consistent with the physical fields in version 1.2 by defining the tracer fields on two time-levels and

Discussion Paper | Discussion Paper | Discussion Paper | Discussion Paper |

GMDD

doi:10.5194/gmd-2015-256

NorESM-OC

J. Schwinger et al.

apply the same time-smoothing procedure as for the physical fields. We anticipate that this improvement will become important on integration time scales of 10 000 years or longer.

2.3.1 Air–sea gas exchange and inorganic carbon chemistry

HAMOCC calculates the exchange of various gases through the air–sea interface. This exchange is determined by three components: The gas solubility in seawater, the gas transfer rate, and the gradient of the gas partial pressure between the atmosphere and the ocean surface. The solubilities of O_2 and N_2 in seawater as functions of surface ocean temperature and salinity are taken from Weiss (1970), and solubilities of CO_2 and N_2O from Weiss and Price (1980). Solubilities of sulfur hexaflouride (SF_6) and the two chlorofluorocarbons CFC-11 and CFC-12 are calculated according to Warner and Weiss (1985) and Bullister et al. (2002). The gas transfer rates are computed using the empirical relationship $k = aU_{10}^2(660/Sc)^{1/2}$ derived by Wanninkhof (1992), where U_{10} is the surface wind speed at 10 m reference height and a is a gas independent constant. The Schmidt number Sc is the kinematic viscosity divided by the diffusivity of the respective gas component, and 660 is the Schmidt number of seawater at 20 °C. Schmidt numbers for CO_2 and CFCs have been taken from Wanninkhof (1992). Since the polynomial used there to fit the experimental data displays non-physical behaviour outside the validity range of the fit for temperatures > 30 °C (very small and negative Schmidt numbers), we use the re-fitted temperature dependence recommended by Gröger and Mikolajewicz (2011) in model version 1.2. The Schmidt number for O_2 is taken from Keeling et al. (1998), and the same value is assumed also for N_2 and N_2O. The model has no gas exchange through ice-covered surface areas of a grid cell, and for partly ice-covered grid cells the gas exchange flux is scaled to the ice free fraction of the cell.

Compared to the original HAMOCC (Maier-Reimer et al., 2005), our model includes a revised inorganic seawater carbon chemistry following Dickson et al. (2007). Total al-

GMDD

doi:10.5194/gmd-2015-256

NorESM-OC

J. Schwinger et al.

kalinity (TA) is defined to include contributions of boric acid, phosphoric acid, hydrogen sulphate, hydrofluoric acid, and silicic acid,

$$TA = [HCO_3^-] + 2[CO_3^{2-}] + [B(OH)_4^-] + [OH^-] + [HPO_4^{2-}] + 2[PO_4^{3-}] + [SiO(OH_3)^-]$$
$$- [H^+] - [HSO_4^-] - [HF] - [H_3PO_4]. \tag{1}$$

The oceanic partial pressure of CO_2 (pCO_2) in the model is prognostically computed as a function of temperature, salinity, dissolved inorganic carbon (DIC), and TA, and the effect of pressure on the various dissociation constants is calculated according to Millero (1995).

2.3.2 Ecosystem model

HAMOCC5 employs an NPZD-type (nutrient, phytoplankton, zooplankton and detritus) ecosystem model, extended to include dissolved organic carbon (DOC). The ecosystem model was initially implemented by Six and Maier-Reimer (1996). The nutrient compartment is represented by three macronutrients (phosphate, nitrate, silicate), and one micronutrient (dissolved iron). A constant Redfield ratio of $P : C : N : O_2 = 1 : 122 : 16 : -172$ following Takahashi et al. (1985) is used. The phytoplankton growth rate $J(I,T)$ follows the light-saturation curve formulation by Smith (1936)

$$J(I,T) = \frac{\alpha\sigma I(z)f(T)}{\sqrt{(\alpha\sigma I(z))^2 + f(T)^2}} \tag{2}$$

with temperature dependence parameterised according to Eppley (1972), $f(T) = \mu_{phy}1.066^T$. Here, $\alpha = 0.02$ is the initial slope of the photosynthesis vs. irradiance curve, $\sigma = 0.4$ is the fraction of photosynthetically active radiation, and $\mu_{phy} = 0.6d^{-1}$. The available light is calculated based on incoming solar radiation prescribed through the atmospheric forcing (I_0) and attenuation through seawater (k_w) and chlorophyll (k_{chl})

$$I(z) = I_0\,e^{-(k_w+k_{chl}Chl)z}. \tag{3}$$

Discussion Paper | Discussion Paper | Discussion Paper | Discussion Paper |

GMDD

doi:10.5194/gmd-2015-256

NorESM-OC

J. Schwinger et al.

Chlorophyll (Chl) is calculated from phytoplankton mass assuming a constant carbon to chlorophyll ratio $R_{C:Chl} = 60$.

A disadvantage of an isopycnic model is the low vertical resolution in weakly stratified regions. The mixed layer in MICOM was represented by only one model layer in Assmann et al. (2010). For NorESM a second model layer has been added to improve the simulation of mixed layer processes. The top model layer varies in thickness between 5 and 10 m while the second model layer represents the rest of the mixed layer. Consequently, for deep mixed layers, the second model layer will often have a vertical extent of 100 m and more, which still results in a rather poor resolution for the simulation of biological processes. We therefore decided to re-implement Eq. (3) for NorESM-OC1.2 by calculating the average light availability $\bar{I}$ (instead of using the light availability at the centre of layers), which reads for layer i:

$$\bar{I}_i = I_{0,i} \frac{1}{(k_w + k_{chl}\text{Chl}_i)\Delta z_i} \left(1 - e^{-(k_w + k_{chl}\text{Chl}_i)\Delta z_i}\right) \tag{4}$$

In addition to light limitation, phytoplankton growth is co-limited by availability of phosphate, nitrate, and dissolved iron. Aerial dust deposition to the surface ocean is prescribed based on Mahowald et al. (2006). A fraction of the dust deposition (3.5 %) is assumed to be iron, and part of it is immediately dissolved and available for biological production. In nitrate-limited regions, i.e. if $[NO_3] < R_{N:P}[PO_4]$, the model assumes nitrogen fixation by cyanobacteria in the surface layer. The distribution of calcium carbonate and biogenic silica production depends on the availability of silicic acid, since it is implicitly assumed that diatoms out-compete other phytoplankton species when supply of silicic acid is sufficient. This is parameterised by assuming that a fraction $[Si]/(K_{Si} + [Si])$ of export production contains opal shells while the remaining fraction contains calcareous shells, where K_{Si} is the half-saturation constant for silicate uptake (Martin-Jézéquel et al., 2000). Phytoplankton loss is modeled by specific mortality and exudation rates as well as zooplankton consumption. DOC is produced by phytoplankton and zooplankton (through constant exudation and excretion rates) and is

Discussion Paper | Discussion Paper | Discussion Paper | Discussion Paper

GMDD

doi:10.5194/gmd-2015-256

NorESM-OC

J. Schwinger et al.

remineralised at a constant rate (whenever the required oxygen is available). The full set of differential equations defining the ecosystem can be found in Maier-Reimer et al. (2005).

Between model version 1 and 1.2 we performed a re-tuning of the ecosystem parameterisation (see Table 2 for old and new parameter values). The objective of this effort was to (i) reduce previously overestimated primary production in high latitudes, (ii) increase production in the low latitude oligotrophic gyres, and (iii) reduce a low latitude bias in alkalinity and DIC found in model version 1. Points (i) and (ii) were addressed by increasing zooplankton abundance (decreasing zooplankton mortality λ_{zoo} and increasing zooplankton assimilation efficiency ω_{zoo}), which helps to limit primary production in the high latitude "high-nutrient, low-chlorophyll" regions. Further, phytoplankton growth is stimulated mainly at low latitudes by reducing the half-saturation constant K_{PO_4} and by increasing available nutrients in the surface by slightly increasing the remineralisation of detritus and DOC. The alkalinity and related DIC bias (iii) were addressed by reducing the surface concentration of silicate in order to increase $CaCO_3$ production. This was done by increasing the opal to phosphorus uptake ratio $R_{Si:P}$.

2.3.3 Particle export and sinking

The standard HAMOCC scheme for the treatment of sinking particles assumes a prescribed constant sinking speed for three classes of particles. Particulate organic carbon associated with dead phytoplankton and zooplankton is transported vertically at $5\,\mathrm{m\,d^{-1}}$. As POC sinks, it is remineralised at a constant rate and according to oxygen availability. When oxygen concentration falls below a threshold of $0.5\,\mathrm{\mu mol\,L^{-1}}$, POC is remineralised by denitrification. Without explicitly modeling this process, it is assumed that 115 moles of nitrate are consumed by denitrifying bacteria to remineralise an amount of detritus corresponding to one mole of phosphate. Particulate inorganic carbon (calcium carbonate, PIC) and opal shells (biogenic silica) sink with a fixed speed of $30\,\mathrm{m\,d^{-1}}$. Biogenic silica is decomposed at depth with a constant dissolution rate while the dissolution of calcium carbonate shells depends on the saturation state

GMDD

doi:10.5194/gmd-2015-256

NorESM-OC

J. Schwinger et al.

with respect to $CaCO_3$ in the surrounding seawater. Non-remineralised particulate materials reaching the sea floor sediment undergo chemical reactions with the sediment pore waters and vertical advection within the sediment. The 12-layer sediment model (Heinze et al., 1999; Maier-Reimer et al., 2005) is primarily relevant for long-term simulations (> 1000 years). Nevertheless, the sediment model was activated for all simulations presented here. The current model version neither includes a parameterisation of weathering fluxes nor does it take into account the influx of carbon and nutrients through continental discharge.

In NorESM-OC1.2 we provide two alternative options for the treatment of particle sinking. First, a scheme which calculates the sinking speed as a linear function of depth as $w_{POC} = \min(w_{min} + a\,z, w_{max})$ has been implemented. Here, w_{min} is the minimum sinking speed found at $z = 0$, and a is a constant describing the increase of speed with depth. The sinking speed can be limited through setting the parameter w_{max}. We refer to this scheme as WLIN in the following text. Note that for $w_{min} = 0$ and $w_{max} = \infty$, this parameterisation is equivalent to the widely used Martin-curve formulation (Martin et al., 1987; Kriest and Oschlies, 2008).

The second new option is a scheme with variable (prognostic) sinking speed which is calculated according to a size distribution of sinking particles. Since an explicit representation of sinking particles through a large number of discrete size classes would not be feasible in a large scale Earth system model due to computational constraints, we implemented the particle aggregation and sinking scheme devised by Kriest and Evans (1999) and Kriest (2002) as a cost effective alternative. This model (hereafter abbreviated KR02) assumes that phytoplankton and detritus form sinking aggregates and that the size distribution of aggregates obeys a power law formulation

$$n(d) = A\,d^{-\varepsilon}, \quad l < d < \infty, \tag{5}$$

where d is the particle diameter, and A and ε are parameters of the distribution. The lower bound of diameters l conceptually corresponds to the size of a single cell. Large values of ε (a steeper slope of the distribution) correspond to a larger number of slow

[GMDD](#)

doi:10.5194/gmd-2015-256

NorESM-OC

J. Schwinger et al.

sinking small particles. By integration over the size range from l to ∞ the total number of aggregates (NOS) is obtained

$$\text{NOS} = A \int_l^\infty d^{-\varepsilon}\,\mathrm{d}d = A\frac{l^{(1-\varepsilon)}}{(\varepsilon-1)}, \tag{6}$$

provided that $\varepsilon > 1$. The mass of an aggregate is described by Cd^ζ and consequently, the total mass of aggregates reads

$$M = A\,C_l\frac{l^{(1-\varepsilon)}}{(\varepsilon-1-\zeta)} = \text{PHY} + \text{POC}, \tag{7}$$

where $C_l = Cl^\zeta$ is the mass of a single cell. If particles were spheres with constant density, then $\zeta = 3$. Since the mass of aggregates grows more slowly than the cube of their diameter, we adopt the value $\zeta = 1.62$ used in Kriest (2002). Finally, it is assumed that the sinking speed of aggregates depends on the diameter according to $w(d) = Bd^\eta$ with $w_l = Bl^\eta$ being the sinking speed of a single cell. The total phytoplankton and detritus mass $M = \text{PHY} + \text{POC}$ and the number of aggregates NOS are the prognostic variables of the KR02-scheme as implemented in HAMOCC. Given M and NOS, the parameters ε and A of the particle size distribution can be determined, and from these the average sinking speed for mass and numbers are obtained.

Aggregation of particles decreases ("flattens") the slope ε of the particle size spectrum, because it reduces the number of particles, but not mass. Sinking removes preferentially the large particles and leaves behind the smaller ones, thereby steepening the slope of the size spectrum in surface layers. These processes are parameterised as in scenario "pSAM" of Kriest (2002), but with stickiness set to 0.25, the factor for shear collisions set to $0.75\,\mathrm{d}^{-1}$, and a maximum particle size for size dependent aggregation and sinking of 0.5 cm (see Table 3 for a summary of parameter values). We assume that all other biogeochemical processes do not impact ε, the exception being

Discussion Paper | Discussion Paper | Discussion Paper | Discussion Paper |

GMDD

doi:10.5194/gmd-2015-256

NorESM-OC

J. Schwinger et al.

zooplankton mortality, which flattens the size spectrum through the addition of (large) zooplankton carcasses.

An implicit scheme is used to redistribute mass (and the number of particles in the case of KR02) through the water column

$$C_i^{t+dt} = C_i^t + \frac{dt}{\Delta z_i}(w_{i-1}C_{i-1}^{t+dt} - w_i C_i^{t+dt}),\tag{8}$$

where dt is the time-step length, Δz_i the thickness of layer i, C stands for the concentration of POC, PIC, opal or NOS, and w_i is the corresponding sinking speed. This scheme is used with prognostic or prescribed sinking speed options. Note that in the KR02 scheme w is a function of time and would be evaluated at time-level $t + dt$ in a fully implicit discretisation. This, however, is practically impossible and we resort to the common simplification of evaluating w at the old time-level ("lagging the coefficients", Anderson, 1995) for the purpose of solving Eq. (8). We further note that PIC and opal are sinking at a fixed prescribed rate of $30\,md^{-1}$ if the standard or WLIN scheme is used, but are assumed to sink as a component of the phytoplankton-detritus aggregates in the KR02 scheme (i.e. at the prognostic sinking speed calculated by the scheme).

2.4 Model configuration

We discuss three different model grid configurations, one for NorESM-OC1, which runs on a displaced pole grid with 1.125° horizontal resolution along the equator and with grid singularities over Antarctica and Greenland. NorESM-OC1.2 has been set up on a numerically more efficient tripolar grid in 1 and 2° nominal resolution. The tripolar grid has its singularities at the South Pole, in Canada, and in Siberia. Due to the more evenly distributed grid spacing of the tripolar grid the time-step can be increased from 1800 to 3200 s, and a timestep of 5400 s can be used for the 2° configuration. We use the abbreviations Mv1, Mv1.2, and Lv1.2 for the three versions/configurations, where "M" and "L" refer to medium (1°) and low (2°) resolution, respectively, followed by the version

Discussion Paper | Discussion Paper | Discussion Paper | Discussion Paper | Discussion Paper |

[GMDD](#)

doi:10.5194/gmd-2015-256

NorESM-OC

J. Schwinger et al.

number of the model. All variants of NorESM-OC discussed here are configured with 51 isopycnic layers referenced at 2000 db and potential densities ranging from 28.202 to 37.800 kg m^{-3}. The reference pressure at 2000 dbar provides reasonable neutrality of model layers in large regions of the ocean (McDougall and Jackett, 2005).

2.4.1 Forcing

Two variants of the data sets developed for the Coordinated Ocean-ice Reference Experiments (COREs, Griffies et al., 2009), the CORE normal year forcing (CORE-NYF, Large and Yeager, 2004) and the CORE interannual forcing (CORE-IAF, Large and Yeager, 2009) can be used to provide the atmospheric forcing for NorESM-OC. Both data sets are based on the NCEP reanalysis (Kalnay et al., 1996) and a number of observational data sets. Corrections are applied to the NCEP surface air temperature, wind, and humidity to remove known biases while precipitation and radiation fields are derived entirely from satellite observations (see Large and Yeager, 2004, 2009 for details). The near surface atmospheric state has a 6 hourly frequency, while the radiation and precipitation fields are daily and monthly means, respectively. The normal year forcing has been constructed to represent a climatological mean year with a smooth transition between the end and start of the year (Large and Yeager, 2004). This forcing can be applied repeatedly for as many years as needed to force an ocean model without imposing interannual variability or discontinuities. We use this forcing data set to spin up our model. The CORE-IAF consists of the corrected NCEP data for the years 1948–2009. Radiation and precipitation data sets are daily and monthly climatological means before 1984 and 1979, respectively, and vary interannually for the time period thereafter.

Since we wish to run hindcast simulations up to present date, but the CORE-IAF only covers the years 1948 to 2009, we devised an alternative data set, which is identical to the CORE-IAF for surface air temperature, wind, humidity, and density (i.e., the same corrections as for the CORE-IAF are applied to the NCEP reanalysis data), but the radiation and precipitation fields are taken from the NCEP reanalysis without any cor-

GMDD

doi:10.5194/gmd-2015-256

NorESM-OC

J. Schwinger et al.

rections. NCEP surface air temperature and specific humidity are re-referenced from 2 to 10 m reference height following the same procedure as used for the CORE forcings (S. Yeager, personal communication, 2012). We refer to this forcing data set as NCEP-C-IAF in the following text.

5 Continental freshwater discharge is based on the climatological annual mean data set described by Dai and Trenberth (2002). It has been modified to include a 0.073 Sv contribution from Antarctica as estimated by Large and Yeager (2009). This freshwater discharge is distributed evenly along the coast of Antarctica as a liquid freshwater flux.

In order to stabilise the model solution we apply salinity relaxation towards observed 10 surface salinity with a restoring time scale of 365 days (version 1) and 350 days (version 1.2) for a 50 m thick surface layer. The restoring is applied as a salt flux which is also present below sea ice. In model version 1.2 balancing of the global salinity relaxation flux was added as an option, which allows to keep the global mean salinity constant over long integration times. That is, positive (negative) relaxation fluxes (where "pos-15 itive" means a salt flux into the ocean) are increased (decreased) by a multiplicative factor if the global total of the relaxation flux is negative (positive). Another option introduced in version 1.2 is a weaker salinity relaxation over the Southern Ocean south of 55° S with a linear ramp between 40 and 55° S. This measure can slightly improve the simulated Southern Ocean hydrography and tracer distributions. Both new options 20 have been activated for all simulations with model version 1.2 presented here, and a time scale of 1050 days has been used for SSS relaxation south of 55° S.

2.4.2 Initialisation and simulation set-up

The physical ocean model is initialised with zero velocities and the January mean temperature and salinity fields from the Polar Science Center Hydrographic Climatology 25 (PHC) 3.0 (Steele et al., 2001). Initial concentrations for the biogeochemical tracers phosphate, silicate, nitrate and oxygen are taken from the gridded climatology of the World Ocean Atlas 2009 (WOA, Garcia et al., 2010a, b). DIC and alkalinity initial values are derived from the GLODAP climatology (Key et al., 2004), using the estimate of an-

GMDD

doi:10.5194/gmd-2015-256

NorESM-OC

J. Schwinger et al.

thropogenic DIC included in the data base to obtain a preindustrial DIC field. In regions of no data coverage a global mean profile of the respective data is used to initialise the model. Dissolved iron concentration is set to 0.6 µmol m^{-3} on initialisation. In the sediment module, the pore water tracers are set to the concentration of the corresponding tracer at the bottom of the water column, and the solid sediment layers are filled with clay only on initialisation.

The model is spun up for 800 (version 1) and 1000 years (version 1.2) using the CORE normal year forcing and an atmospheric CO_2 concentration of 278 ppm corresponding to preindustrial values to get the oceanic tracers into a near-equilibrium state. The spin-up time span is still too short to attain full equilibrium, but the strong initial transient changes in tracer concentrations following the initialisation flatten out after about 500 years simulation time. During the last 100 years of the spin-up carbon fluxes (positive into the ocean) stabilised at 0.26, 0.005, and 0.004 Pg C yr^{-1}, with only small trends of 0.00007, 0.021, and −0.048 Pg C yr^{-1} century^{-1} for Mv1, Mv1.2, and Lv1.2, respectively.

Following the spin-up, we initialise two hindcast runs for each model version and configuration. The "historical" run uses prescribed atmospheric CO_2 concentrations taken from the data set provided by Le Quéré et al. (2015). We start model integrations on 1 January 1762, since atmospheric CO_2 begins to exceed the spinup value of 278 ppm in this year. The second hindcast, which we call "natural" run in this text, is continued with the constant preindustrial CO_2 concentration of 278 ppm. Northern and Southern Hemisphere tropospheric concentrations of CFC-11, CFC-12, and SF_6 are prescribed according to Bullister (2014). The historical and natural simulations continue to be forced by the CORE normal year forcing until 1947. At 1 January 1948 we branch off historical and natural runs that are forced by CORE and NCEP-C interannually varying forcing (two historical and two natural runs for each model version and configuration). In the following sections we focus mainly on the simulations forced with the NCEP-C-IAF data set, and all results presented have been obtained with this forcing unless explicitly stated otherwise.

GMDD

doi:10.5194/gmd-2015-256

NorESM-OC

J. Schwinger et al.

3   Results and discussion

3.1   Physical model

3.1.1   Temperature and salinity

Zonal mean temperature (T) and salinity (S) differences between model and the obser-
5 vation based climatology from WOA 2009 (Locarnini et al., 2010; Antonov et al., 2010)
for the Atlantic and Pacific basins are shown in Figs. 1 and 2. The general patterns of
T and S deviations are similar across the different model versions and configurations.
Note that Mv1 did not apply a balancing of the salinity relaxation flux. Since the unbal-
anced salinity relaxation flux removes salt from the model in all three configurations,
10 the average salinity in Mv1 decreased by about 0.2 psu during the course of the inte-
gration. The predominantly negative salinity bias for the Mv1 configuration is visible in
Fig. 2. The mid-latitude and tropical regions have a too strong temperature gradient in
the upper 700 m, that is, a warm bias in the upper thermocline and a cold bias below.
While magnitude and extent of the warm bias are similar for the three model configu-
15 rations (up to ≈ 4 °C), the cold bias is weakest for Mv1, and strongest (up to −4 °C) for
the low resolution configuration Lv1.2.

In the Southern Ocean south of 50° S, the model is generally biased towards too cold
and fresh conditions (about −1 to −2 °C and up to −0.5 psu) below a slightly too warm
surface layer. The layer of upwelled Atlantic deep water, which is warmer and more
20 saline than Southern Ocean surface waters, is not or only weakly preserved in the
model. At depths below 3000–4000 m the cold and fresh bias extends northwards into
the Atlantic basin up to the equator (a weak cold bias extends into the North Atlantic
at depth). Above these bottom water masses and below the thermocline the Atlantic
is generally too warm by 1 to 2 °C and too saline by 0.2 to 0.5 psu (again, salinity is
25 biased low in Mv1 due to the unbalanced salinity restoring flux). In contrast, a warm
and saline bias at intermediate depths in the Pacific is mostly confined to the Southern
Hemisphere, whereas the North Pacific is biased cold and fresh at all depths below

GMDD

doi:10.5194/gmd-2015-256

NorESM-OC

J. Schwinger et al.

Discussion Paper | Discussion Paper | Discussion Paper | Discussion Paper |

1000 m for all model configurations. We note that the cold and fresh bias in the Southern Ocean water column is specific to the stand-alone configuration of the model and is not found in the fully coupled version of NorESM (e.g. Bentsen et al., 2013, Fig. 14).

3.1.2 Atlantic Meridional Overturning Circulation

5   The Atlantic Meridional Overturning Circulation (AMOC) for the ocean-ice only configuration of Mv1.2 has been compared to results from other models in Danabasoglu et al. (2014). The forcing protocol for this latter study was to run the model through five cycles (1948–2007) of the CORE-IAF. The AMOC strength in our model, measured as the maximum of the annual mean meridional stream-function at 26.5° N, varied between
10   12.5 and 19 Sv and showed an increasing trend of roughly 1 Sv century^{-1}. Under the spin-up with the CORE-NY forcing performed in the present work, the AMOC shows a long transient increase in strength for about 300 years before stabilising. The average overturning for the 30 years before switching to inter-annual forcing (1918–1947) is 22.3, 24.8, and 21.5 Sv for Mv1, Mv1.2, and Lv1.2 respectively (triangles in Fig. 3).
15   Aside from the absolute values we find similar curves of AMOC strength under the forcing protocol applied here (Fig. 3) compared to the results presented in Danabasoglu et al. (2014): first a 10 to 15 year decrease by 2 to 4 Sv followed by a relatively stable phase until the early 1980s, an increase by 4 to 7 Sv towards a maximum in the late 1990s and another decrease until the end of the simulation period (2007 or 2014). The
20   Lv1.2 configuration forced by NCEP-C-IAF is an outlier in our small model ensemble. Compared to the other model simulations there is a negative trend in AMOC strength of 8 Sv over the simulation period, but the curve appears to be similar to the others if this trend would be removed.

In model configuration Mv1 we find only minor differences in AMOC strength between
25   the simulation forced with CORE-IAF and the one forced with NCEP-C-IAF. For Mv1.2 and Lv1.2, however, the CORE-IAF simulations show a weaker initial decrease and a generally larger overturning than the corresponding NCEP-C-IAF simulations. These differences can be traced back to a peculiarity of the salinity relaxation scheme when

GMDD

doi:10.5194/gmd-2015-256

NorESM-OC

J. Schwinger et al.

Interactive Discussion

the balancing of the relaxation flux is activated (not available in model version 1). Since too much salt is taken out of the surface ocean globally by the unbalanced scheme, negative salt fluxes are reduced by a multiplicative factor when balancing of the salinity relaxation flux is activated. Interestingly, the global restoring salt flux imbalance is larger

5   when the model is forced with the CORE-IAF. As a consequence of correcting this imbalance, we find a stronger reduction of restoring salt flux out of the surface ocean in the simulations performed with CORE-IAF compared to those forced with NCEP-C-IAF. In the Atlantic north of 40° N a positive salinity bias is therefore reinforced in the CORE-IAF simulations with model version 1.2, driving an increase of the AMOC relative to the

10 simulations forced with NCEP-C-IAF. We note that AMOC strength has been estimated as 17.2 Sv for the time period from April 2004 to October 2012 based on observations from the Rapid Climate Change programme (RAPID) array (McCarthy et al., 2015). Compared to this value our model overestimates AMOC strength by about 4 to 9 Sv, except for the special case of Lv1.2 forced with NCEP-C-IAF discussed above, where

15 AMOC is lower than the observational estimate by about 2 Sv for the period 2004 to 2012.

3.1.3   Mixed layer depth and CFC-11

Seasonal cycles of modelled average bulk mixed layer depth (MLD) compared to the climatology of de Boyer Montégut et al. (2004) are shown for several regions in Fig. 4.

20 We find a good agreement of modelled and observation based MLD in terms of phasing and summer minimum depth, whereas during autumn and winter modelled average MLDs are up to 40 to 100 m larger outside the tropics. The largest differences are found in the Southern Ocean south of 60° S (Fig. 4f) during austral winter. However, the observation based climatology relies on very few profiles during May–October in

25 this region. Further, our calculation of model average MLD excluded ice covered grid cells while we have no information about how many observed profiles taken under ice cover in the Antarctic entered the climatology. We therefore have little confidence in the model–data comparison for the southernmost Southern Ocean during winter.

GMDD

doi:10.5194/gmd-2015-256

NorESM-OC

J. Schwinger et al.

In the tropics modelled average MLDs are roughly 20 m larger than observed year round (i.e. about 60 vs. 40 m) with a small annual cycle that corresponds well to the data based estimate. Generally, the three model versions and configurations show very similar average MLD, but the low resolution configuration Lv1.2 has a less pronounced
5   seasonal cycle (i.e. the winter maximum MLD is shallower and hence closer to the observation based estimate).

MLD averaged over large regions and time periods is not necessarily a useful indicator of upper ocean ventilation since spatially and temporarily localised convection events can transport vertically large amounts of heat and matter. In fact, the mod-
10 elled maximum MLD is frequently larger than 800 m over extended areas of the Southern Ocean (not shown). The zonal mean distribution of CFC-11 in model version 1.2 (Fig. 5) clearly indicates a too deep mixing when compared to observed CFC-11 profiles from the GLODAP data base. In the Atlantic sector of the Southern Ocean between 500 to 1000 m depth we find relatively high average CFC-11 concentrations
15 of up to $3 \, \mathrm{nmol \, m^{-3}}$, whereas the corresponding observed CFC-11 concentration is $0.44 \, \mathrm{nmol \, m^{-3}}$. We note that forcing the model with the NCEP-C-IAF data set tends to attenuate the deep mixing in the Southern Ocean compared to simulations carried out with the CORE-IAF (see Fig. 5c). In the North Atlantic we find frequent deep convection with maximum MLDs as deep as 1400 m in the Labrador and Irminger Sea as
20 well as in the Greenland and Norwegian Sea. The comparison with GLODAP CFC-11 data reveals a tendency for high CFC-11 concentrations located at too large depths also in the Labrador and Irminger Sea (GLODAP does not cover the Nordic Seas). In mid latitudes we find less CFC-11 in central and intermediate water masses, best seen as a negative bias in the modelled zonal mean integrated CFC-11 content (Fig. 5e)
25 between 40° S and 40° N.

3.2   Primary production

Differences between version 1 and 1.2 of NorESM-OC are to a large extent due to differences in the ecosystem parameter settings. We compare model results with satel-

GMDD

doi:10.5194/gmd-2015-256

NorESM-OC

J. Schwinger et al.

Discussion Paper | Discussion Paper | Discussion Paper | Discussion Paper |

lite derived estimates of primary production (PP), which are based on MODIS data and an Eppley-Vertically Generalized Production Model (Eppley-VGPM, Behrenfeld and Falkowski, 1997). We processed ten years of these data (2003–2012; obtained from www.science.oregonstate.edu/ocean.productivity) into a climatology as detailed in Appendix. We note that the Eppley-VGPM algorithm produces global PP estimates at about the mean value of different models that calculate depth-integrated primary production from satellite measurements of ocean colour (Carr et al., 2006).

Figure 6 shows the mean PP over the years 2003–2012 for the model configurations Mv1, Mv1.2, and Lv1.2 and the satellite based climatology. As noted in Sect. 2.3.2, model version 1 has a very strong PP at high latitudes, a feature that is not found in the satellite derived estimate. Values are high in excess of $10\,\mathrm{mol\,C\,m^{-2}\,yr^{-1}}$ almost everywhere south of 40° S and north of 40° N (Fig. 6a and e). These large discrepancies are reduced in model version 1.2 through the re-tuning of the ecosystem model described in Sect. 2.3.2. A positive bias with respect to the Eppley-VGPM is still found in the North Pacific and south of 40° S, but differences are reduced to less than $5\,\mathrm{mol\,C\,m^{-2}\,yr^{-1}}$. In the Atlantic north of 40° N large scale average PP outside of the shelf regions compares well with with the Eppley-VGPM in model version 1.2, although PP appears to be slightly lower than the Eppley-VGPM estimate in the Greenland and Norwegian Seas.

In lower latitudes (40° S to 40° N) outside of equatorial and coastal upwelling regions, all three model versions and configurations show a rather low production. Since this region represents a large area of the world ocean, the global integrated PP is lower than the VGPM-estimate of $56.9\,\mathrm{Pg\,C\,yr^{-1}}$ for all model configurations (46.0 for Mv1, 37.0 for Mv1.2, and $31.2\,\mathrm{Pg\,C\,yr^{-1}}$ for Lv1.2). Figures 6e and 7 show that this discrepancy indeed originates in the latitudes between 40° S and 40° N. Despite the ecosystem re-tuning and the lower nutrient consumption in the Southern Ocean in model version 1.2, PP is only slightly higher in Mv1.2 compared to Mv1 (and about equal in Lv1.2). We conclude that rather than caused by inadequate ecosystem parameter settings, the modelled low PP at low latitudes is caused by a too low nutrient supply from below the euphotic zone, due to too stably stratified water masses (warm bias at the surface, cold

GMDD

doi:10.5194/gmd-2015-256

NorESM-OC

J. Schwinger et al.

GMDD

doi:10.5194/gmd-2015-256

NorESM-OC

J. Schwinger et al.

bias in the lower thermocline, Fig. 1). The lower PP in the low resolution is consistent with the stronger cold bias found in this configuration. The model does not show elevated PP in most shelves regions (aside from upwelling systems), since the shelves are only poorly resolved in the model, particularly in the lower resolution configuration. This missing PP on the shelves contributes to the rather low total PP in the model compared to the VGPM estimate.

The mean seasonal cycle of vertically integrated PP (averaged over the years 2003–2012) is shown in Fig. 8 for six regions. The too strong productivity in model Mv1 is reflected in a very pronounced productivity peak in late spring or early summer everywhere south of 40° S and north of 40° N. Model version 1.2 shows a significantly reduced annual cycle of PP in these regions (approximately 40–80 % reduction of peak production), much better in line with the VGPM based PP estimates. In the North Atlantic and North Pacific the peak production of $30\,\mathrm{mol\,C\,m^{-2}\,yr^{-1}}$ in the updated model comes close to the VGPM value. In the southern high latitude region (60 to 40° S) the modelled PP also peaks at about $30\,\mathrm{mol\,C\,m^{-2}\,yr^{-1}}$, but here the corresponding VGPM estimates are much lower (peaking at $10\,\mathrm{mol\,C\,m^{-2}\,yr^{-1}}$). In late summer, autumn, and winter modelled PP at high latitudes is lower than the observational estimate.

In the tropics and subtropics the annual cycle of PP shows little difference between model versions (Figs. 8c and d). In the southern subtropics (20 to 40° S, very similar results for the northern subtropics) we find a too strong seasonal cycle as well, with production peaking in early Southern Hemisphere spring (October/November) in the model, while the VGPM shows maximum PP in summer. In contrast, the phasing of minimum PP is the same in the model and the VGPM estimate (occurring in late autumn/early winter). We note that the modelled phasing of the southern subtropical production maximum coincides better with the satellite based PP data product by Nevison et al. (2015, not shown).

3.3 Biogeochemical tracers

3.3.1 Nutrients

Maps of surface phosphate concentrations for the three model versions and configurations Mv1, Mv1.2, and Lv1.2 as well as the observation based global climatology from
WOA 2009 (Garcia et al., 2010b) are shown in Fig. 9. The reduced high latitude PP in model version 1.2 leads to larger surface phosphate concentrations almost everywhere north of 40° N and south of 40° S compared to Mv1. This improves the agreement with observations (i.e. reduces the negative PO_4 bias found in Mv1) in the Southern Ocean and in the North Pacific. In contrast, a positive PO_4 bias is introduced in the North
Atlantic north of 40° N in model version 1.2. In the Southern Ocean simulated PO_4 surface concentrations are closest to observations in the configuration Lv1.2.

In all model versions/configurations there is too much phosphate trapped at intermediate depth in the tropical oxygen minimum zones, while there is a negative bias below approximately 2000 m depth as well as in the whole water column of the Southern Ocean. This general pattern is shown for the Atlantic in Fig. 10 but is also found in the other ocean basins. Besides the broad similarities, a considerable redistribution of phosphate at depth can be observed across the different model configurations. Due to the lower PP in the Southern Ocean in model version 1.2 less phosphate is trapped south of 50° S and more phosphate is found in the oxygen minimum zones of
the tropical oceans. A similar redistribution of nutrients in the world oceans in response to a changed export production in the Southern Ocean has been reported for other models earlier (e.g. Sarmiento and Orr, 1991; Marinov et al., 2006; Primeau et al., 2013).

To investigate the different phosphate distributions further, we plot preformed phosphate in Fig. 11. Here, we approximate preformed phosphate by $PO_4^{pref} \approx PO_4 -$ $AOU/R_{O_2:P}$ (Broecker et al., 1985, where $R_{O_2:P} = 172$ is the stoichiometric oxygen to phosphorus ratio used in the model), since a preformed phosphate tracer was not

Discussion Paper | Discussion Paper | Discussion Paper | Discussion Paper |

GMDD

doi:10.5194/gmd-2015-256

NorESM-OC

J. Schwinger et al.

GMDD

doi:10.5194/gmd-2015-256

NorESM-OC

J. Schwinger et al.

available in version 1 of the model, and because we can estimate preformed phosphate from WOA observations in the same manner. The differences between the approximation and the explicitly simulated preformed tracer (available in version 1.2) are relatively small in the Atlantic where anaerobic remineralisation of POC is not abundant in the model. The preformed phosphate concentrations are very similar in Mv1 and Mv1.2 south of 50° S. Hence, the stronger negative bias in total PO_4 found in Mv1.2 is indeed caused by a smaller remineralised fraction. The too strong PP in Mv1 in the Southern Ocean also results in too low preformed phosphate concentrations in Antarctic Intermediate Waters. This bias is clearly reduced in model version 1.2 since less nutrients are stripped out of surface waters by biological production in the Southern Ocean. Likewise, the increased surface PO_4 concentration in model version 1.2 in the Atlantic north of 40° N leads to higher than observed preformed phosphate concentrations in intermediate and deep waters in the Atlantic basin.

The modelled distribution of nitrate (not shown) is similar to phosphate in terms of biases and general spatial structure since the model uses a fixed stoichiometric ratio ($R_{N:P}$ = 16) for the composition of organic matter. Moreover, nitrogen fixation, which occurs in the surface ocean as soon as $[NO_3] < R_{N:P}[PO_4]$, acts towards preserving the assumed stoichiometric ratio of the two nutrients. Major differences are found in the oxygen minimum zones, where NO_3 is consumed to remineralise organic matter and produce PO_4 during denitrification. This effect is particularly pronounced in the tropical Pacific where the modelled oxygen minimum zones are excessively large (see below). Here, we find a local minimum of nitrate instead of a local maximum as observed and as it is found for phosphate.

Surface silicate concentrations (Fig. 12) in the Southern Ocean are much lower than observed in Mv1. Larger Si concentrations and hence a better agreement with observations are simulated with model version 1.2 due to the reduced PP in the Southern Ocean. Again (as for maximum PO_4 concentrations) the maximum Si values are closest to observations in Lv1.2. The lower surface silicate concentrations equatorward of approximately 35° in version 1.2 compared to version 1 is maintained (despite the

Discussion Paper | Discussion Paper | Discussion Paper | Discussion Paper

much lower Si consumption in the Southern Ocean) due to the re-tuned silicate uptake (increased $R_{Si:P}$). Although the concentration differences are not large, particularly not relative to the half-saturation constant for silicate uptake ($K_{Si} = 1\,\mathrm{mmol\,Si\,m^{-3}}$), the effect over more than 1000 years of integration is a clear reduction of alkalinity in model version 1.2 (see below) due to a slightly but constantly larger fraction of calcareous shell formation.

Generally, the global spatial surface concentration pattern of silicate is less well reproduced than the surface pattern of PO_4 in all model configurations. The area of high silicate concentration around Antarctica is broader (i.e. extents further north) than observed and the observed north–south asymmetry with much smaller values in the northern high latitudes (north of 40° N) is not well reproduced either. This might indicate that our ecosystem model is not tuned well enough or that its structure is oversimplified with respect to silicate sources and sinks.

A summary of model skill for surface and interior distributions of nutrients is given in the Taylor-diagrams shown in Fig. 13. Surface ocean nitrate and phosphate show high correlations with observed fields ($R > 0.9$ except for PO_4 in Mv1 where $R = 0.87$) and a good agreement of spatial variability. Spatial variability is lowest in Mv1 due to the underestimation of surface PO_4 and NO_3 concentrations at high latitudes. Highest skill scores are found for Lv1.2 consistent with the fact that this model configuration comes closest to observed surface concentrations in the Southern Ocean. Simulated surface silicate fields show significantly lower correlations with observations (between $R = 0.5$ for Mv1 and $R = 0.8$ for Lv1.2). Spatial Si variability is too high for model version 1.2 because of the too large Si surface concentration north of 40° N, while Mv1 reproduces the observed surface Si variability, however with a wrong spatial pattern.

The improved simulation of surface nutrients in model version 1.2 comes at the cost of less model skill in the interior ocean (Fig. 13b–d). Apparently, the too strong PP in the Southern Ocean in Mv1 partly compensates for deficiencies in the circulation field. As discussed above, a larger Southern Ocean PP increases the amount of phosphate trapped in the water column south of 50° S and reduces the amount of phosphate

[GMDD](#)

doi:10.5194/gmd-2015-256

NorESM-OC

J. Schwinger et al.

trapped in the tropical oxygen minimum zones in version 1 compared to version 1.2 (Fig. 10). Hence, model version 1.2 shows less correlation and a larger variability of PO_4 at 500 m depth. Simulated nitrate fields at this depth level are modified by denitrification. Since the tropical oxygen minimum zones are considerably larger than observed, particularly in the Pacific, model skill with respect to NO_3 is reduced.

The dominant impact of the oxygen minimum zones on model skill at 500 m depth can be assessed by restricting the analysis to the extra-tropical ocean (i.e., by omitting grid points located between 20° S and 20° N, Fig. 13d). Then, phosphate variability is very close to observed, and the correlation of modelled nitrate with observations increases by almost 0.3 for all model configurations such that it becomes similar to that of phosphate.

At 2000 m depth skill scores for Mv1 and Mv1.2 are similar for the three nutrients. Lv1.2 reaches better skill scores (or about equal for silicate) than the higher resolution configurations. Silicate has a rather uniform distribution at this depth, and is reproduced well by all configurations, leading to relative high skill scores for Si.

3.3.2 Oxygen

As discussed in Sect. 3.1 there is too much deep convection and associated tracer transport to depth in the Southern Ocean in all model versions and configurations. Oxygen is particularly affected, since O_2 solubility at cold temperatures is high (this is also true for CO_2, but the upwelled water masses in the Southern Ocean tend to be rich in DIC and low in oxygen). During the long simulations (more than 1000 years) presented here the deep ocean fills up with oxygen rich waters originating from the Southern Ocean. The resulting zonal mean O_2 concentrations along a section through the central Pacific and the differences with respect to the WOA 2009 climatology (Garcia et al., 2010a) are shown in Fig. 14. In the Southern Ocean south of 50° S and at depths deeper than 500 m we find an average positive bias of 0.05, 0.1, and 0.09 mol m^{-3} in Mv1, Mv1.2, and Lv1.2, respectively. The much lower bias in model configuration Mv1 is due to the larger flux of organic matter from the surface ocean. We find average AOU

GMDD

doi:10.5194/gmd-2015-256

NorESM-OC

J. Schwinger et al.

Discussion Paper | Discussion Paper | Discussion Paper | Discussion Paper

values of 0.09, 0.04, and 0.05 mol m^{-3} (average south of 50° S at depths deeper than 500 m), such that preformed O$_2$ is virtually exactly the same for all model versions and configurations. We note that part of the deep ocean oxygen bias is connected to low POC transport into the deep ocean below 2000 m when the standard sinking scheme
5   is used. This is further discussed in Sect. 3.5.

The modelled oxygen minimum zones (OMZs) are excessively large in all model versions and configurations. This is particularly true for the Pacific basin (Fig. 14), and to a lesser degree for the tropical Atlantic and tropical Indian Ocean (not shown). The impact of the parameterisation of POC sinking on the modelled OMZs is discussed in
10   Sect. 3.5.

3.3.3 Dissolved inorganic carbon and alkalinity

Surface maps of DIC and alkalinity for the three model configurations and the corresponding data based GLODAP climatologies are shown in Figs. 15 and 16. Model version 1 has a strong positive bias in DIC and alkalinity, which is most pronounced
15   between approximately 40° S and 50° N. This bias is driven by a too large production of alkalinity in these latitudes. In our model, alkalinity is (aside from advection and diffusion) governed by biological production, which adds one mole alkalinity per mole nitrate consumed, and calcium carbonate production, which decreases alkalinity by 2 moles per mole CaCO$_3$ produced (Wolf-Gladrow et al., 2007). Since the partitioning
20   between opal and CaCO$_3$ production is parameterised dependent on available silicate, the reduction of surface silicate concentrations at low latitudes in model version 1.2 (Sect. 3.3.1) results in increased CaCO$_3$ production and a considerable reduction of the alkalinity and DIC biases. Average surface DIC concentrations in the Southern Ocean are lowest for Mv1.2. Again, as in the case of phosphate, the reason for this
25   is a lower remineralised concentration of DIC in the upwelled water masses compared to Mv1, and a lower preformed DIC concentration compared to Lv1.2 (not shown, but compare Figs. 10 and 11).

GMDD

doi:10.5194/gmd-2015-256

NorESM-OC

J. Schwinger et al.

Discussion Paper | Discussion Paper | Discussion Paper | Discussion Paper |

GMDD

doi:10.5194/gmd-2015-256

NorESM-OC

J. Schwinger et al.

3.4 Oceanic pCO$_2$, ocean carbon sink, and anthropogenic carbon

Compared to the observation based data product of Landschützer et al. (2015a, b) we find that the general pattern of surface CO$_2$ partial pressure in sea water (pCO$_2$, Fig. 17) is well reproduced by the model. The pCO$_2$ maximum at low latitudes is
5 broader and less confined to the equatorial region than observed. The main factors contributing to this mismatch are the very high primary production in the narrow eastern equatorial Pacific upwelling band (compare Fig. 6), which draws down pCO$_2$ in the model where it has its maximum in observations, and the higher than observed values in the upwelling areas along the west coast of America and Africa. In the southernmost
10 Southern Ocean modeled mean pCO$_2$ values are about 30 (Mv1.2) and 15 ppm (Lv1.2) lower than in the Landschützer et al. (2015a) data product. This is consistent with the DIC and alkalinity distributions found in this region (see Figs. 15 and 16). We note that there are only small differences between a multiannual mean of the Landschützer et al. (2015a) data and the Takahashi et al. (2009) pCO$_2$ climatology.
15 We finally use the historical and natural runs to estimate the contemporary ocean carbon sink as well as the total storage of anthropogenic carbon (DIC$_{ant}$) in the ocean. The ocean carbon sink is defined here as the carbon flux including its natural variability corrected for the mean and trend found in the natural simulation. This flux is calculated for the recent decades from 1959 to 2013 with the starting date 1959 chosen such
20 that any shock due to the change of atmospheric forcing in 1948 has vanished and does not influence the calculation of trends. Results for the different model versions and configurations forced with NCEP-C-IAF and CORE-IAF are shown in Fig. 18. The simulated ocean carbon sink is largest for model version 1 with a mean carbon sink of 2.58 and 2.50 Pg C yr^{-1} during 1990 to 1999 when forced with the NCEP-C-IAF
25 and CORE-IAF, respectively. The accumulated uptake over 1959 to 2007 for this model version and the two forcing data sets differs in the same proportion (102 vs. 99 Pg C). Model version 1.2 shows a lower ocean carbon sink with a mean value of 2.33 Pg C yr^{-1} over the 1990 to 1999 period for the medium resolution configuration (2.46 when forced

with CORE-IAF). The corresponding numbers for the low resolution simulation forced with the NCEP-C and CORE-IAF are 2.01 and 2.24 $Pg\,C\,yr^{-1}$, respectively. We compare these model results to the three independent data based estimates (grey symbols with error bars in Fig. 18) of McNeil et al. (2003), $2.0 \pm 0.4\,Pg\,C\,yr^{-1}$ over 1990–1999,

5 Manning and Keeling (2006), $1.9 \pm 0.6\,Pg\,C\,yr^{-1}$ over 1990–2000, and Mikaloff Fletcher et al. (2006), $2.2 \pm 0.25\,Pg\,C\,yr^{-1}$ for 1995, which are the basis for the ocean sink value given in the Intergovernmental Panel on Climate Change Fourth Assessment Report (Denman et al., 2007), and which are also used as the data based ocean sink estimate in Le Quéré et al. (2015). The simulated ocean sink appears to be too large in

10 Mv1 while for version 1.2 the sink estimates are within the error bars of the data based estimates. The closest match is found for the low resolution configuration forced with NCEP-C-IAF which has the lowest carbon uptake. The rather too high CO_2 uptake is confirmed when comparing the model results to the CO_2 flux estimates of Landschützer et al. (2015a). There is a relatively good agreement with the CO_2 sink simulated with

15 Lv1.2 up to 1990 and towards the end of the time series (year 2011). From the early 1990s until 2001 the Landschützer et al. (2015a) data shows a marked decline followed by a steep increase of carbon uptake, which they attribute to a saturation followed by a reinvigoration of the Southern Ocean carbon sink. Although our model also shows a stagnation of the ocean carbon sink during the 1990s there is no pronounced min-

20 imum and hence a rather large deviation from the Landschützer et al. (2015a) data around the year 2000.

  The anthropogenic dissolved inorganic carbon (DIC_{ant}) stored in the ocean is displayed in Fig. 19. Consistent with the larger than observed carbon sink fluxes our model also shows higher anthropogenic carbon storage compared to the Sabine et al. (2004)

25 estimate of DIC_{ant} available from the GLODAP data base. In the North Atlantic modeled anthropogenic carbon is larger than observed, which is consistent with the too strong simulated AMOC. Model version 1.2 has a larger AMOC when simulations are forced with the CORE-IAF (see Sect. 3.1.2), and we find a larger accumulation of DIC_{ant} in the North Atlantic for this forcing (not shown) consistent with the larger (accumulated)

GMDD

doi:10.5194/gmd-2015-256

NorESM-OC

J. Schwinger et al.

uptake flux (Fig. 18). In the Southern Ocean the too high concentration of DIC_{ant} is consistent with the too strong ventilation diagnosed from the CFC-11 tracer (Sect. 3.1.3). Larger than observed DIC_{ant} concentrations are also found north of 40° S where DIC is subducted in Antarctic Intermediate Waters.

3.5 Particle export and sedimentation

To evaluate the three different sinking schemes available in NorESM-OC1.2, we conducted a spin-up run over 1000 years for each scheme using the low-resolution configuration of the model. In addition we performed one sensitivity experiment employing the standard option, but with the constant POC sinking speed increased from 5 to 14 m d^{-1}. These two runs are referred to as STD-slow and STD-fast, respectively, while the model runs employing the prognostic particle aggregation scheme (Kriest, 2002) and the linear increase of sinking speed are abbreviated KR02 and WLIN in the following text. The parameter settings used for the KR02 aggregation scheme can be found in Table 3, and we use $w_{min} = 7\,\text{m d}^{-1}$, $w_{max} = 43\,\text{m d}^{-1}$, and $a = 40/2500\,\text{m d}^{-1}\text{m}^{-1}$ for the run WLIN. The global average sinking speed profiles for the four experiments are shown in Fig. 20a.

Faster sinking particles provide a more efficient removal of carbon and nutrients from the surface ocean. Therefore, the amount of PP would drop considerably in STD-fast, KR02, and WLIN compared to the standard parameterisation if no other measures taken. Since already the PP of about 30 Pg C yr^{-1} found for Lv1.2 is at the low end of observation based estimates (Carr et al., 2006), and since we wish to have a similar PP in the four configurations as a starting point for our evaluation, we tune the ecosystem parameterisation for the runs STD-fast, KR02, and WLIN towards less efficient export and more efficient recycling of nutrients in the euphotic zone. This is accomplished by reducing both the fraction of grazing egested $(1-e_{zoo})$ and the assimilation efficiency of herbivores ω_{zoo} (see Table 2), a measure which reduces the fraction of grazing routed to detritus and increases the fraction that is recycled directly to phosphate (see Maier-Reimer et al., 2005, Eqs. 9 and 11). At the end of the spin-up runs we find globally

GMDD

doi:10.5194/gmd-2015-256

NorESM-OC

J. Schwinger et al.

integrated PP values of 29.6, 29.0, 28.4, and 30.4 Pg C yr^{-1} for the experiments STD-slow, STD-fast, KR02, and WLIN.

Figure 20b shows the average POC fluxes at 100 and 2000 m depth, and at the ocean bottom (where water depth is larger than 1000 m) for the four experiments and recent observation based estimates of these fluxes (Henson et al., 2012; Honjo et al., 2008; Laws et al., 2000; Seiter et al., 2005). The carbon export fluxes (POC flux through 100 m depth) of 4.0 to 5.6 Pg C yr^{-1} found in the model are at the lower end of observation based estimates (4 to 11.2 Pg C yr^{-1}). The three runs employing the differently tuned ecosystem show a lower export than the STD-slow configuration. Note that in the KR02 scheme living phytoplankton is part of the sinking aggregates (in STD and WLIN phytoplankton does not sink), hence the relative large export despite the re-tuned ecosystem. The POC flux through 2000 m is significantly smaller than the observed range in STD-slow (0.16 vs. 0.43 to 0.66 Pg C yr^{-1}), while it falls within or slightly above this range for the other three runs (0.45, 0.69, and 0.68 Pg C yr^{-1} for STD-fast, KR02, and WLIN, respectively). A similar picture emerges for the bottom POC flux: In STD-slow it is again much smaller than the Seiter et al. estimate (0.03 vs. 0.5 Pg C yr^{-1}), while the other sinking schemes yield values which are more comparable (though smaller: 0.17, 0.32, and 0.36 Pg C yr^{-1} for STD-fast, KR02, and WLIN, respectively). We will evaluate the POC flux at 2000 m in more detail below.

Since the absolute POC fluxes depend on PP, and estimates of PP derived from satellite data differ widely, we plot the export ratio or export efficiency (EE, defined as F_{100}^{POC}/PP, where F_{100}^{POC} is the POC flux at 100 m depth) as well as the transfer efficiency (TF, defined as $F_{2000}^{POC}/F_{100}^{POC}$) in Fig. 20c. The global average export efficiency in all four model runs (STD-slow 18 %, STD-fast 14 %, KR02 21 %, and WLIN 14 %) falls within the range estimated based on observations (10 to 21 %). Consistent with the results for the absolute fluxes, the transfer efficiency obtained for STD-slow is too small in comparison to the observational estimates (1.7 % vs. 7.5 to 19 %), while the other runs fall within this range (STD-fast 9 %, KR02 10 %, and WLIN 16 %). These results indicate that the flux reaching the deep ocean below 2000 m and the sediments is likely too low

Discussion Paper | Discussion Paper | Discussion Paper | Discussion Paper |

GMDD

doi:10.5194/gmd-2015-256

NorESM-OC

J. Schwinger et al.

in the STD-slow configuration. Regarding the three other schemes, a conclusion is difficult to draw, since the spread in the observation based estimates is large.

The global zonal mean distribution of remineralised phosphate ($PO_4^{remin} = PO_4 - PO_4^{pref}$, where PO_4^{pref} is calculated based on AOU as above) shown in Fig. 21 reveals that there is a strong negative bias in the STD-slow simulations everywhere below 2000 m, and also at shallower depth in the Southern Ocean and north of 40° N. This bias is reduced if one of the three other sinking schemes is used, but the reduction is only weak in the deep ocean for STD-fast. A strong positive bias of PO_4^{remin} is found in intermediate water masses at tropical and subtropical latitudes as well as in the tropical oxygen minimum zones for the STD-slow scheme. This bias is not significantly reduced in the STD-fast experiment, but there is a clear reduction found in KR02 and WLIN. Out of the three schemes with more efficient sinking KR02 appears to perform slightly better in terms of PO_4^{remin} bias, while STD-fast clearly has less skill than KR02 and WLIN. We note that improvements in simulated PO_4^{remin} directly translate into improved oxygen fields. The positive O_2 bias discussed in Sect. 3.3.2 is reduced in the deep ocean if one of the more efficient sinking schemes is employed. E.g., below 3000 m depth average O_2 biases are 0.1 mol m^{-3} for STD-slow, 0.07 for STD-fast, and 0.06 for both KR02 and WLIN. Oxygen minimum zones are also better simulated in KR02 and WLIN, particularly in the Atlantic, whereas the improvement in the Pacific basin is modest.

We further evaluate the sinking schemes by comparison with a comprehensive synthesis of sediment trap data published by Honjo et al. (2008). These data have been normalised to 2000 m depth and comprise 134 stations of which we consider 120 here. We do not use ten stations for which the closest model grid point has a depth of less than 2000 m, and we disregard two stations in the high Arctic and two in the Mediterranean. Further, we form the mean value of fluxes for stations situated in the same model grid cell leaving us with 102 model-data pairs. The scatter diagrams presented in Fig. 22 confirm the too low flux of POC in STD-low. POC fluxes at 2000 m in this model configuration are smaller than 0.05 mol C m^{-2} yr^{-1} for all but eight stations in the

GMDD

doi:10.5194/gmd-2015-256

NorESM-OC

J. Schwinger et al.

Discussion Paper | Discussion Paper | Discussion Paper | Discussion Paper |

tropical Pacific. The latter stations are located in the narrow equatorial tongue of excessively high PP (compare Fig. 6). In this region we find the too large oxygen minimum zones at depth, where remineralisation by oxygen ceases and is replaced by less efficient processes (denitrification, sulphate reduction). As mentioned above the choice of the sinking scheme does not significantly improve the excessive oxygen minimum zones in the Pacific. Therefore, we also find some very high POC fluxes inconsistent with observations in STD-fast, KR02, and WLIN at tropical Pacific sites (Fig. 22b, c, and d).

STD-fast shows modeled POC fluxes through 2000 m depth that are still clearly too small. Except for a few sites located in the tropical Pacific fluxes are smaller than $0.2\,mol\,C\,m^{-2}\,yr^{-1}$ whereas observed values range up to $0.6\,mol\,C\,m^{-2}\,yr^{-1}$ in the Arabian Sea. One could argue that a further increase of the constant sinking speed would probably further improve the modeled fluxes. However, a constant sinking speed very efficiently removes POC and associated particular nutrients from the upper ocean. Already the $14\,m\,d^{-1}$ constant sinking speed is faster in the upper 500 m of the water column than the sinking speed in KR02 and WLIN (Fig. 20a). A significant increase of the constant sinking speed would therefore require a strong further tuning of ecosystem parameters towards more recycling and less efficient export to keep PP in the range of observed values. This would lead to even smaller values for export efficiency inconsistent with observation based estimates.

The KR02 scheme is able to reproduce the highest POC flux values, which have been observed in the Arabian Sea (orange dots in Fig. 22). This might be unsurprising, since the KR02 parameterisation has been originally developed and tested for application in this region. However, the scheme simulates also rather large flux values ($> 0.5\,mol\,C\,m^{-2}\,yr^{-1}$) for three nearby stations in the tropical Indian Ocean (yellow dots in Fig. 22) and one station in the subtropical Atlantic (blue dots) where the corresponding observed values are between 0.1 and $0.3\,mol\,C\,m^{-2}\,yr^{-1}$. At the low end of observed flux values, the KR02 scheme is able to reproduce the lowest observed flux values well, but there are too many low POC flux values simulated by the scheme,

GMDD

doi:10.5194/gmd-2015-256

NorESM-OC

J. Schwinger et al.

mainly in the Southern Ocean south of 60° S (red dots), in the Atlantic north of 40° N (dark blue dots), and in the tropical Atlantic (light blue dots).

The WLIN scheme does not yield any fluxes larger than $3.2\,\mathrm{mol\,C\,m^{-2}\,yr^{-1}}$ outside the tropical Pacific, that is, the highest observed POC fluxes in the Arabian Sea are not well reproduced. Also, the scheme does not produce any fluxes smaller than $0.02\,\mathrm{mol\,C\,m^{-2}\,yr^{-1}}$. Hence also three of the four smallest observed flux values are better simulated by KR02 than WLIN. The correlations obtained with KR02 and WLIN are 0.32 and 0.22. However, if we omit the high flux stations in the Arabian Sea (station number 54 to 58 in Honjo et al., 2008), we find correlations of 0.23 and 0.28 for KR02 and WLIN, respectively. Hence, the relatively better correlation with sediment trap observations in KR02 compared to WLIN is solely due to better representation of high POC fluxes in the Arabian Sea. Finally we note that if we additionally disregard the stations in the tropical Pacific (stations 103 to 111 in Honjo et al., 2008), where the large discrepancy between model and sediment trap data is due to other model deficiencies than the POC sinking scheme, the correlations increase to 0.44 and 0.52 for KR02 and WLIN.

4   Summary and conclusions

We have evaluated and compared two versions and several configurations of NorESM-OC, the stand-alone ocean carbon-cycle set-up of the Norwegian Earth System Model (NorESM). Model version NorESM-OC1 corresponds to the fully coupled NorESM1-ME, which participated in CMIP5. Important updates made for NorESM-OC1.2 include the implementation of two new sinking schemes for particulate organic carbon (POC), and a re-tuning of the ecosystem parameterisation. We have presented results for different grid configurations (1.125° displaced pole grid for version 1, 1 and 2° tripolar grid for version 1.2) and two slightly different forcing data sets (CORE and NCEP-C).

The re-tuning of the ecosystem parameterisation reduces primary production (PP) in high latitudes in model version 1.2, which significantly improves agreement with ob-

Discussion Paper | Discussion Paper | Discussion Paper | Discussion Paper |

GMDD

doi:10.5194/gmd-2015-256

NorESM-OC

J. Schwinger et al.

servation based PP estimates. Also, simulation results for surface nutrients, dissolved inorganic carbon, and alkalinity are improved. On the other hand, model skill in the deeper ocean is slightly deteriorated. Particularly in the Southern Ocean, the stronger trapping of nutrients and the larger consumption of oxygen for remineralisation due to the too high PP in version 1 partly compensate for deficiencies in the circulation field.

We find that the deep ventilation in the Southern Ocean is too strong in the model, such that, over the long integration times considered here, too much oxygen accumulates in the Southern Ocean and in deep waters ventilated from there. In the tropical ocean, particularly in the Pacific, the model develops too large oxygen minimum zones along with a too strong accumulation of remineralised phosphate.

The ocean carbon sink as simulated with the model (using the standard POC sinking scheme) ranges from 2.01 to 2.58 Pg C yr^{-1} for the time period 1990–1999. The higher value stems from version 1 of the model and lies above the error bars of estimates based on observations. Version 1.2 of the model generally simulates a lower carbon uptake more in line with the observational estimates. We find only a weak sensitivity of our ocean sink estimate to the forcing data used, an exception being the low resolution configuration of version 1.2 forced with the NCEP-C data set. For this configuration, a reduced ocean circulation (reduced AMOC) translates to a reduced carbon uptake (the lower end of the range given above).

Results of the simulations with different sinking parameterisations indicate that the standard sinking scheme used in our model so far (constant sinking speed, constant remineralisation rate) fails to transport enough carbon into the deep ocean, even if the sinking speed is increased considerably. The two new options implemented in version 1.2 (linear increase of sinking speed with depth, and a particle aggregation scheme, which calculates sinking speed prognostically) show much better agreement with sediment trap data at 2000 m depth. Deep ocean biases of remineralised phosphate (too low in the model) and O_2 (too high in the model) are reduced significantly, e.g., the average O_2 bias below 3000 m depth is reduced from 0.1 to 0.06 mol m^{-3} for both new sinking parameterisations compared to the standard scheme.

GMDD

doi:10.5194/gmd-2015-256

NorESM-OC

J. Schwinger et al.

Based on the evaluation presented in this work, there is no definite conclusion as to which of the two new POC sinking schemes performs better in our model. The examination of remineralised phosphate is slightly in favour of the particle aggregation scheme, which is also able to reproduce the highest recorded POC fluxes through 2000 m at stations in the Arabian sea. On the other hand, the bulk of sediment trap measurements is slightly better reproduced by simply assuming that sinking speed increases linearly with depth. From a conceptual point of view, the aggregation scheme introduces additional parameters which are only poorly constrained by observational studies. Also, the prognostic particle aggregation depends on the number and mass of particles and consequently on primary production, which still is a quantity with large uncertainties in both the model and observational estimates. Obviously, the specification of a global sinking speed profile requires less parameters, but regional differences due to different ecosystem structure cannot be represented.

There are several directions for future model development that can be identified from our results. The tropical oxygen minimum zones are a long standing problem to be solved. The hope that a more realistic parameterisation of POC sinking would also result in an improved simulation of oxygen minimum zones in our model, particularly in the Pacific, has not been fulfilled. Part of this problem is the distribution of primary production which is too high in a narrow band along the upwelling water masses in the tropical Pacific and too low in the neighboring oligotrophic subtropical gyres, leading to a wrong distribution of particle rain. Simulations with increased spatial resolution will help to elucidate which improvements can be made through a more accurate representation of ocean currents in this region.

Future higher resolution model configurations will also offers the opportunity to study processes in shelf regions in more detail, where currently neglected processes are likely to be of importance. These include the parameterisation of tidal mixing induced sediment–water column interactions, and a fully consistent representation of the inflow of carbon and nutrients through rivers.

GMDD

doi:10.5194/gmd-2015-256

NorESM-OC

J. Schwinger et al.

Discussion Paper | Discussion Paper | Discussion Paper | Discussion Paper |

In the Southern Ocean, we need to address temperature and salinity biases connected to deficiencies in the circulation field as well as the problem of too much deep ventilation. Due to the long integration time scales needed to spin-up the biogeochemistry module of our model, errors in the Southern Ocean circulation and ventilation can result in extended biases in the interior ocean, e.g., the deep ocean O_2 bias seen in the model simulations presented here. Further, the rather high modeled anthropogenic carbon uptake originates (partly) in the Southern Ocean, and improvements of these estimates are urgently needed to help better constraining the carbon budget of the Earth system.

Appendix A: Climatology of satellite derived primary production

The satellite climatology was constructed from monthly gridded PP data for the years 2003–2012 that were obtained from the Ocean Productivity Website (www.science. oregonstate.edu/ocean.productivity). These data are derived from MODIS retrievals using the Eppley-VGPM algorithm (Behrenfeld and Falkowski, 1997). From these PP estimates (original resolution 1/6 of a degree) we first assembled a monthly climatology on a $1° \times 1°$ grid with the requirement that a grid point should have valid data for at least 3 out of 10 years. From this monthly climatology we finally arrive at the annual climatology by averaging over all months. In the last step we assume that grid points without data are not observed due to unfavorable light conditions, and therefore assume zero production there. This procedure might lead to an underestimation of PP in the satellite based climatology at high latitudes ($> 50°$).

Code availability

We are committed to share NorESM with the scientific community and to make the model available for scientific and educational purposes. As major model components are based on software developed by others, whose interests have to be protected,

GMDD

doi:10.5194/gmd-2015-256

NorESM-OC

J. Schwinger et al.

availability of the code is subject to signing a license agreement. Please mail to noresm-ncc@met.no for inquiries about obtaining the source code of NorESM. For the use of HAMOCC signing of the MPI-ESM license agreement is required in addition, which can be easily done through http://www.mpimet.mpg.de/en/science/models/

5 model-distribution.html

Acknowledgements. J. Schwinger, N. Goris, I. Bethke, M Ilicak, and M. Bentsen were supported by the Research Council of Norway through project EVA (229771), and J. Tjiputra acknowledges the Research Council of Norway funded project ORGANIC (239965/RU). Supercomputer time and storage resources were provided by the Norwegian metacenter for computa-
10 tional science (NOTUR, project nn2980k), and the Norwegian Storage Infrastructure (NorStore, project ns2980k). This work was supported by the Bjerknes Centre for Climate Research. We gratefully acknowledge the CESM project, which is supported by the National Science Foundation and the Office of Science (BER) of the US Department of Energy. Mixed layer depth climatologies based on observed profiles have been obtained from the IFREMER/LOS Mixed
15 Layer Depth Climatology website www.ifremer.fr/cerweb/deboyer/mld.

References

Anderson, J.: Computational Fluid Dynamics, McGraw-Hill, Inc., New York, USA, 1995. 14

Antonov, J., Seidov, D., Boyer, T., Locarnini, R., Mishonov, A., Garcia, H., Baranova, O., Zweng, M., and Johnson, D.: Salinity, in: World Ocean Atlas 2009, Volume 2, edited by: Levitus, S.,
20 NOAA Atlas NESDIS 70, U.S. Government Printing Office, Washington, D.C., USA, 184 pp., 2010. 18

Assmann, K. M., Bentsen, M., Segschneider, J., and Heinze, C.: An isopycnic ocean carbon cycle model, Geosci. Model Dev., 3, 143–167, doi:10.5194/gmd-3-143-2010, 2010. 3, 7, 10

Behrenfeld, M. and Falkowski, P.: Photosynthetic rates derived from satellite-based chlorophyll
25 concentration, Limnol. Oceanogr., 42, 1–20, 1997. 22, 38

Bentsen, M., Bethke, I., Debernard, J. B., Iversen, T., Kirkevåg, A., Seland, Ø., Drange, H., Roelandt, C., Seierstad, I. A., Hoose, C., and Kristjánsson, J. E.: The Norwegian Earth System Model, NorESM1-M – Part 1: Description and basic evaluation of the physical climate, Geosci. Model Dev., 6, 687–720, doi:10.5194/gmd-6-687-2013, 2013. 3, 5, 19

GMDD

doi:10.5194/gmd-2015-256

NorESM-OC

J. Schwinger et al.

Discussion Paper | Discussion Paper | Discussion Paper | Discussion Paper |

Bleck, R. and Smith, L. T.: A wind-driven isopycnic coordinate model of the North and Equatorial Atlantic Ocean, 1. Model development and supporting experiments, J. Geophys. Res., 95, 3273–3285, 1990. 3, 5

Bleck, R., Rooth, C., Hu, D., and Smith, L.: Salinity-driven thermocline transients in a wind- and thermohaline-forced isopycnic coordinate model of the North Atlantic, J. Phys. Oceanogr., 22, 1486–1505, 1992. 3, 5

Bretherton, F.: Earth system science and remote sensing, Proc. IEEE, 73, 1118–1127, 1985. 3

Broecker, W. S., Takahashi, T., and Takahashi, T.: Sources and Flow Patterns of Deep-Ocean Waters as Deduced From Potential Temperature, Salinity, and Initial Phosphate Concentration, J. Geophys. Res., 90, 6907–6924, 1985. 24

Bullister, J.: Updated (2014) Atmospheric CFC-11, CFC-12, CFC-113, CCl4 and SF6 Histories, available at: http://cdiac.ornl.gov/ftp/oceans/CFC_ATM_Hist/CFC_ATM_Hist_2014, last access: 5 December 2014. 17

Bullister, J. L., Wisegarver, D. P., and Menzia, F. A.: The solubility of sulfur hexafluoride in water and seawater, Deep-Sea Res. Pt. I, 49, 175–187, 2002. 8

Carr, M.-E., Friedrichs, M. A. M., Schmeltz, M., Aita, M. N., Antoine, D., Arrigo, K. R., Asanuma, I., Aumont, O., Barber, R., Behrenfeld, M., Bidigare, R., Buitenhuis, E. T., Campbell, J., Ciotti, A., Dierssen, H., Dowell, M., Dunne, J., Esaias, W., Gentili, B., Gregg, W., Groom, S., Hoepffner, N., Ishizaka, J., Kameda, T., Le Quere, C., Lohrenz, S., Marra, J., Melin, F., Moore, K., Morel, A., Reddy, T. E., Ryan, J., Scardi, M., Smyth, T., Turpie, K., Tilstone, G., Waters, K., and Yamanaka, Y.: A comparison of global estimates of marine primary production from ocean color, Deep-Sea Res. Pt. II, 53, 741–770, doi:10.1016/j.dsr2.2006.01.028, 2006. 22, 31

Dai, A. and Trenberth, K.: Estimates of freshwater discharge from continents: Latitudinal and seasonal variations, J. Hydrometeorol., 3, 660–687, 2002. 16

Danabasoglu, G., Yeager, S. G., Bailey, D., Behrens, E., Bentsen, M., Bi, D., Biastoch, A., Böning, C., Bozec, A., Canuto, V. M., Cassou, C., Chassignet, E., Coward, A. C., Danilov, S., Diansky, N., Drange, H., Farneti, R., Fernandez, E., Fogli, P. G., Forget, G., Fujii, Y., Griffies, S. M., Gusev, A., Heimbach, P., Howard, A., Jung, T., Kelley, M., Large, W. G., Leboissetier, A., Lu, J., Madec, G., Marsland, S. J., Masina, S., Navarra, A., Nurser, A. G., Pirani, A., y Mélia, D. S., Samuels, B. L., Scheinert, M., Sidorenko, D., Treguier, A.-M., Tsujino, H., Uotila, P., Valcke, S., Voldoire, A., and Wang, Q.: North Atlantic simulations in coordinated

ocean-ice reference experiments phase II (CORE-II). Part I: Mean states, Ocean Model., 73, 76–107, 2014. 5, 19

de Boyer Montégut, C., Madec, G., Fischer, A. S., Lazar, A., and Iudicone, D.: Mixed layer depth over the global ocean: an examination of profile data and a profile-based climatology, J. Geophys. Res., 109, C12003, doi:10.1029/2004JC002378, 2004. 20, 55

Denman, K. L., Brasseur, G., Chidthaisong, A., Ciais, P., Cox, P. M., Dickinson, R. E., Hauglustaine, D., Heinze, C., Holland, E., Jacob, D., Lohmann, U., Ramachandran, S., da Silva Dias, P. L., Wofsy, S. C., and Zhang, X.: Couplings Between Changes in the Climate System and Biogeochemistry, in: Climate Change 2007: The Physical Science Basis. Contribution of Working Group I to the Fourth Assessment Report of the Intergovernmental Panel on Climate Change, edited by: Solomon, S., Qin, D., Manning, M., Chen, Z., Marquis, M., Averyt, K. B., Tignor, M., and Miller, H. L., Cambridge University Press, Cambridge, UK and New York, NY, USA, 2007. 30

Dickson, A., Sabine, C., and Christian, J.: Guide to Best Practices for Ocean CO_2 Measurements, PICES special publication 3, North Pacific Marine Science Organization (PICES), Sidney, British Columbia, Canada, 2007. 8

Downes, S. M., Farneti, R., Uotila, P., Griffies, S. M., Marsland, S. J., Bailey, D., Behrens, E., Bentsen, M., Bi, D., Biastoch, A., Böning, C., Bozec, A., Canuto, V. M., Chassignet, E., Danabasoglu, G., Danilov, S., Diansky, N., Drange, H., Fogli, P. G., Gusev, A., Howard, A., Ilicak, M., Jung, T., Kelley, M., Large, W. G., Leboissetier, A., Long, M., Lu, J., Masina, S., Mishra, A., Navarra, A., Nurser, A. G., Patara, L., Samuels, B. L., Sidorenko, D., Spence, P., Tsujino, H., Wang, Q., and Yeager, S. G.: An assessment of Southern Ocean water masses and sea ice during 1988–2007 in a suite of interannual CORE-II simulations, Ocean Model., 94, 67–94, 2015. 5

Dukowicz, J. and Baumgardner, J.: Incremental remapping as a transport/advection algorithm, J. Comput. Phys., 160, 318–335, 2000. 5

Eden, C. and Greatbatch, R.: Towards a mesoscale eddy closure, Ocean Model., 20, 223–239, doi:10.1016/j.ocemod.2007.09.002, 2008. 6

Eden, C., Jochum, M., and Danabasoglu, G.: Effects of different closures for thickness diffusivity, Ocean Model., 26, 47–59, doi:10.1016/j.ocemod.2008.08.004, 2009. 6

Eppley, R. W.: Temperature and phytoplankton growth in the sea, Fish. Bull., 70, 1063–1085, 1972. 9

GMDD

doi:10.5194/gmd-2015-256

NorESM-OC

J. Schwinger et al.

Discussion Paper | Discussion Paper | Discussion Paper | Discussion Paper

Farneti, R., Downes, S. M., Griffies, S. M., Marsland, S. J., Behrens, E., Bentsen, M., Bi, D., Biastoch, A., Böning, C., Bozec, A., Canuto, V. M., Chassignet, E., Danabasoglu, G., Danilov, S., Diansky, N., Drange, H., Fogli, P. G., Gusev, A., Hallberg, R. W., Howard, A., Ilicak, M., Jung, T., Kelley, M., Large, W. G., Leboissetier, A., Long, M., Lu, J., Masina, S., Mishra, A., Navarra, A., Nurser, A. G., Patara, L., Samuels, B. L., Sidorenko, D., Tsujino, H., Uotila, P., Wang, Q., and Yeager, S. G.: An assessment of Antarctic Circumpolar Current and Southern Ocean meridional overturning circulation during 1958–2007 in a suite of interannual CORE-II simulations, Ocean Model., 93, 84–120, 2015. 5

Flato, G. M.: Earth system models: an overview, Wiley Interdisciplinary Reviews: Climate Change, 2, 783–800, doi:10.1002/wcc.148, 2011. 3

Fox-Kemper, B., Ferrari, R., and Hallberg, R.: Parameterization of mixed layer eddies, Part I: Theory and diagnosis, J. Phys. Oceanogr., 38, 1145–1165, 2008. 6

Garcia, H., Locarnini, R., Boyer, T., Antonov, J., Baranova, O., Zweng, M., and Johnson, D.: Dissolved oxygen, apparent oxygen utilization, and oxygen saturation, in: World Ocean Atlas 2009, Vol 3., edited by: Levitus, S., NOAA Atlas NESDIS 70, U.S. Government Printing Office, Washington, D.C., USA, 344 pp., 2010a. 16, 27

Garcia, H., Locarnini, R., Boyer, T., Antonov, J., Zweng, M., Baranova, O., and Johnson, D.: Nutrients (phosphate, nitrate, silicate), in: World Ocean Atlas 2009, Vol. 4, edited by: Levitus, S., NOAA Atlas NESDIS 71, U.S. Government Printing Office, Washington, D.C., USA, 398 pp., 2010b. 16, 24, 64

Gent, P., Danabasoglu, G., Donner, L., Holland, M., Hunke, E., Jayne, S., Lawrence, D., Neale, R., Rasch, P., Vertenstein, M., Worley, P., Yang, Z., and Zhang, M.: The Community Climate System Model version 4, J. Climate, 24, 4973–4991, doi:10.1175/2011JCLI4083.1, 2011. 3

Griffies, S., Biastoch, A., Böning, C., Bryan, F., Danabasoglu, G., Chassignet, E., England, M., Gerdes, R., Haak, H., Hallberg, R., Hazeleger, W., Jungclaus, J., Large, W., Madec, G., Pirani, A., Samuels, B., Scheinert, M., Gupta, A., Severijns, C., Simmons, H., Treguier, A., Winton, M., Yeager, S., and Yin, J.: Coordinated Ocean-ice Reference Experiments (COREs), Ocean Model., 26, 1–46, doi:10.1016/j.ocemod.2008.08.007, 2009. 15

Griffies, S. M., Yin, J., Durack, P. J., Goddard, P., Bates, S. C., Behrens, E., Bentsen, M., Bi, D., Biastoch, A., Böning, C. W., Bozec, A., Chassignet, E., Danabasoglu, G., Danilov, S., Domingues, C. M., Drange, H., Farneti, R., Fernandez, E., Greatbatch, R. J., Holland, D. M., Ilicak, M., Large, W. G., Lorbacher, K., Lu, J., Marsland, S. J., Mishra, A., Nurser, A. G., y Mélia, D. S., Palter, J. B., Samuels, B. L., Schröter, J., Schwarzkopf, F. U.,

Sidorenko, D., Treguier, A.-M., heng Tseng, Y., Tsujino, H., Uotila, P., Valcke, S., Voldoire, A., Wang, Q., Winton, M., and Zhang, X.: An assessment of global and regional sea level for years 1993–2007 in a suite of interannual CORE-II simulations, Ocean Model., 78, 35–89, doi:10.1016/j.ocemod.2014.03.004, 2014. 5

5 Gröger, M. and Mikolajewicz, U.: Note on the CO_2 air-sea gas exchange at high temperatures, Ocean Model., 39, 284–290, 2011. 8

Heinze, C., Maier-Reimer, E., Winguth, A., and Archer, D.: A global oceanic sediment model for long-term climate studies, Global Biogeochem. Cy., 13, 221–250, 1999. 12

Henson, S. A., Sanders, R., and Madsen, E.: Global patterns in efficiency of particulate or-
10 ganic carbon export and transfer to the deep ocean, Global Biogeochem. Cy., 26, GB1028, doi:10.1029/2011GB004099, 2012. 32, 71

Holland, M., Bailey, D., Briegleb, B., Light, B., and Hunke, E.: Improved sea ice shortwave radiation physics in CCSM4: The impact of melt ponds and aerosols on Arctic Sea ice, J. Climate, 25, 1413–1430, doi:10.1175/JCLI-D-11-00078.1, 2012. 3, 6

15 Honjo, S., Manganini, S. J., Krishfield, R. A., and Francois, R.: Particulate organic car-
bon fluxes to the ocean interior and factors controlling the biological pump: a syn-
thesis of global sediment trap programs since 1983, Prog. Oceanogr., 76, 217–285, doi:10.1016/j.pocean.2007.11.003, 2008. 32, 33, 35, 71, 73

Hunke, E. and Lipscomb, W.: CICE: the Los Alamos Sea Ice Model, documentation and soft-
20 ware, version 4.0, Tech. Rep. LA-CC-06-012, Los Alamos National Laboratory, Los Alamos, New Mexico, USA, 2008. 6

Ilyina, T., Six, K. D., Segschneider, J., Maier-Reimer, E., Li, H., and Núñez Riboni, I.: Global ocean biogeochemistry model HAMOCC: model architecture and performance as compo-
nent of the MPI-Earth System Model in different CMIP5 experimental realizations, J. Adv.
25 Model. Earth Syst., 5, 287–315, doi:10.1029/2012MS000178, 2013. 7

Kalnay, E., Kanamitsu, M., Kistler, R., Collins, W., Deaven, D., Gandin, L., Iredell, M., Saha, S., White, G., Woollen, J., Zhu, Y., Chelliah, M., Ebisuzaki, W., Higgins, W., Janowiak, J., Mo, K., Ropelewski, C., Leetmaa, A., Reynolds, R., and Jenne, R.: The NCEP/NCAR 40 year reanalysis project, B. Am. Meteorol. Soc., 77, 437–471, 1996. 15

30 Keeling, R., Stephens, B., Najjar, R., Doney, S., Archer, D., and Heimann, M.: Seasonal varia-
tions in the atmospheric O_2/N_2 ratio in relation to the kinetics of air-sea gas exchange, Global Biogeochem. Cyc., 12, 141–163, 1998. 8

GMDD

doi:10.5194/gmd-2015-256

NorESM-OC

J. Schwinger et al.

Key, R., Kozyr, A., Sabine, C., Lee, K., Wanninkhof, R., Bullister, J., Feely, R., Millero, F., Mordy, C., and Peng, T.-H.: A global ocean carbon climatology: Results from GLODAP, Global Bio-geochem. Cyc., 18, GB4031, doi:10.1029/2004GB002247, 2004. 16

Kirkevåg, A., Iversen, T., Seland, Ø., Hoose, C., Kristjánsson, J., Struthers, H., Ekman, A., Ghan, S., Griesfeller, J., Nilsson, E., and Schulz, M.: Aerosol-climate interactions in the Norwegian Earth System Model – NorESM1-M, Geosci. Model Dev., 6, 207–244, doi:10.5194/gmd-6-207-2013, 2013. 3

Kriest, I.: Different parameterizations of marine snow in a 1-D model and their influence on representation of marine snow, nitrogen budget and sedimentation, Deep-Sea Res. Pt. I, 49, 2133–2162, 2002. 12, 13, 31

Kriest, I. and Evans, G.: Representing phytoplankton aggregates in biogeochemical models, Deep-Sea Res. Pt. I, 46, 1841–1859, 1999. 12

Kriest, I. and Oschlies, A.: On the treatment of particulate organic matter sinking in large-scale models of marine biogeochemical cycles, Biogeosciences, 5, 55–72, 2008. 12

Kwon, E. Y., Primeau, F., and Sarmiento, J. L.: The impact of remineralization depth on the air-sea carbon balance, Nat. Geosci., 2, 630–635, doi:10.1038/NGEO612, 2009. 4

Landschützer, P., Gruber, N., and Bakker, D. C. E.: A 30 years observation-based global monthly gridded sea surface pCO2 product from 1982 through 2011, Carbon Dioxide In-formation Analysis Center, Oak Ridge National Laboratory, US Department of Energy, Oak Ridge, Tennessee, USA, available at: http://cdiac.ornl.gov/ftp/oceans/SPCO2_1982_2011_ETH_SOM_FFN, 28 September 2015a. 29, 30, 68, 69

Landschützer, P., Gruber, N., Haumann, A., Rödenbeck, C., Bakker, D. C. E., van Heuven, S., Hoppema, M., Metzl, N., Sweeney, C., Takahashi, T., Tilbrook, B., and Wanninkhof, R.: The reinvigoration of the Southern Ocean carbon sink, Science, 349, 1221–1224, doi:10.1126/science.aab2620, 2015b. 29

Large, W. and Yeager, S.: Diurnal to Decadal Global Forcing for Ocean and Sea-Ice Models: The Data Sets and Flux Climatologies, Tech. Note NCAR/TN-460+STR, National Center of Atmospheric Research, Boulder, Colorado, USA, 2004. 15

Large, W. and Yeager, S.: The global climatology of an interannually varying air-sea flux data set, Clim. Dynam., 33, 341–364, doi:10.1007/s00382-008-0441-3, 2009. 15, 16

Laws, E. A., Falkowski, P. G., Smith Jr., W. O., Ducklow, H., and McCarthy, J. J.: Temperature effects on export production in the open ocean, Global Biogeochem. Cyc., 14, 1231–1246, 2000. 32, 71

GMDD

doi:10.5194/gmd-2015-256

NorESM-OC

J. Schwinger et al.

Le Quéré, C., Moriarty, R., Andrew, R. M., Peters, G. P., Ciais, P., Friedlingstein, P., Jones, S. D., Sitch, S., Tans, P., Arneth, A., Boden, T. A., Bopp, L., Bozec, Y., Canadell, J. G., Chini, L. P., Chevallier, F., Cosca, C. E., Harris, I., Hoppema, M., Houghton, R. A., House, J. I., Jain, A. K., Johannessen, T., Kato, E., Keeling, R. F., Kitidis, V., Klein Goldewijk, K., Koven, C., Landa, C. S., Landschützer, P., Lenton, A., Lima, I. D., Marland, G., Mathis, J. T., Metzl, N., Nojiri, Y., Olsen, A., Ono, T., Peng, S., Peters, W., Pfeil, B., Poulter, B., Raupach, M. R., Regnier, P., Rödenbeck, C., Saito, S., Salisbury, J. E., Schuster, U., Schwinger, J., Séférian, R., Segschneider, J., Steinhoff, T., Stocker, B. D., Sutton, A. J., Takahashi, T., Tilbrook, B., van der Werf, G. R., Viovy, N., Wang, Y.-P., Wanninkhof, R., Wiltshire, A., and Zeng, N.: Global carbon budget 2014, Earth Syst. Sci. Data, 7, 47–85, doi:10.5194/essd-7-47-2015, 2015. 4, 17, 30, 69

Lindsay, K., Bonan, G. B., Doney, S. C., Hoffman, F. M., Lawrence, D. M., Long, M. C., Mahowald, N. M., Moore, J. K., Randerson, J. T., and Thornton, P. E.: Preindustrial-Control and Twentieth-Century Carbon Cycle Experiments with the Earth System Model CESM1(BGC), J. Climate, 27, 8981–9005, doi:10.1175/JCLI-D-12-00565.1, 2014. 3

Locarnini, R., Mishonov, A., Antonov, J., Boyer, T., Garcia, H., Baranova, O., Zweng, M., and Johnson, D.: Temperature, in: World Ocean Atlas 2009, Vol. 1, edited by: Levitus, S., NOAA Atlas NESDIS 70, U.S. Government Printing Office, Washington, D.C., USA, 184 pp., 2010. 18

Mahowald, N. M., Muhs, D. R., Levis, S., Rasch, P. J., Yoshioka, M., Zender, C. S., and Luo, C.: Change in atmospheric mineral aerosols in response to climate: Last glacial period, preindustrial, modern, and doubled carbon dioxide climates, J. Geophys. Res., 111, D10202, doi:10.1029/2005JD006653, 2006. 10

Maier-Reimer, E.: Geochemical cycles in an ocean general circulation model. Preindustrial tracer distributions, Global Biogeochem. Cyc., 7, 645–677, 1993. 3, 7

Maier-Reimer, E., Kriest, I., Segschneider, J., and Wetzel, P.: The Hamburg Oceanic Carbon Cycle Circulation model HAMOCC5.1 – Technical Description Release 1.1, Reports on Earth System Science 14, Max Planck Institute for Meteorology, Hamburg, Germany, 2005. 3, 7, 8, 11, 12, 31, 50

Manning, A. and Keeling, R.: Global oceanic and land biotic carbon sinks from the Scripps atmospheric oxygen flask sampling network, Tellus B, 58, 95–116, doi:10.1111/j.1600-0889.2006.00175.x, 2006. 30, 69

GMDD

doi:10.5194/gmd-2015-256

NorESM-OC

J. Schwinger et al.

Marinov, I., Gnanadesikan, A., Toggweiler, J. R., and Sarmiento, J. L.: The Southern Ocean biogeochemical divide, Nature, 441, 964–967, doi:10.1038/nature04883, 2006. 4, 24

Martin, J., Knauer, G., Karl, D., and Broenkow, W.: VERTEX: Carbon cycling in the Northeast Pacific, Deep-Sea Res., 34, 267–285, 1987. 12

5 Martin-Jézéquel, V., Hildebrand, M., and Brzezinski, M. A.: Silicon metabolism in diatoms: implications for growth, J. Phycol., 36, 821–840, 2000. 10

McCarthy, G., Smeed, D., Johns, W., Frajka-Williams, E., Moat, B., Rayner, D., Baringer, M., Meinen, C., Collins, J., and Bryden, H.: Measuring the Atlantic meridional overturning circulation at 26° N, Prog. Oceanogr., 130, 91–111, doi:10.1016/j.pocean.2014.10.006, 2015.
10 20

McDougall, T. and Jackett, D.: An assessment of orthobaric density in the global ocean, J. Phys. Oceanogr., 35, 2054–2075, doi:10.1175/JPO2796.1, 2005. 15

McNeil, B., Matear, R., Key, R., Bullister, J., and Sarmiento, J.: Anthropogenic CO_2 uptake by the ocean based on the global chlorofluorocarbon data set, Science, 299, 235–239,
15 doi:10.1126/science.1077429, 2003. 30, 69

Mikaloff Fletcher, S., Gruber, N., Jacobson, A., Doney, S., Dutkiewicz, S., Gerber, M., Follows, M., Joos, F., Lindsay, K., Menemenlis, D., Mouchet, A., Muller, S., and Sarmiento, J.: Inverse estimates of anthropogenic CO_2 uptake, transport, and storage by the ocean, Global Biogeochem. Cyc., 20, GB2002, doi:10.1029/2005GB002530, 2006. 30, 69

20 Millero, F. J.: Thermodynamics of the carbon dioxide system in the oceans, Geochim. Cosmochim. Ac., 59, 661–677, 1995. 9

Nevison, C. D., Manizza, M., Keeling, R. F., Kahru, M., Bopp, L., Dunne, J., Tiputra, J., Ilyina, T., and Mitchell, B. G.: Evaluating the ocean biogeochemical components of Earth system models using atmospheric potential oxygen and ocean color data, Biogeosciences, 12, 193–
25 208, doi:10.5194/bg-12-193-2015, 2015. 23

Oberhuber, J. M.: Simulation of the Atlantic circulation with a coupled sea ice-mixed layer-isopycnal general circulation model, Part I: Model description, J. Phys. Oceanogr., 23, 808–829, 1993. 6

Primeau, F. W., Holzer, M., and DeVries, T.: Southern Ocean nutrient trapping and the efficiency
30 of the biological pump, J. Geophys. Res., 118, 2547–2564, doi:10.1002/jgrc.20181, 2013. 24

Sabine, C., Feely, R., Gruber, N., Key, R., Lee, K., Bullister, J., Wanninkhof, R., Wong, C., Wallace, D., Tilbrook, B., Millero, F., Peng, T., Kozyr, A., Ono, T., and Rios, A.: The oceanic

GMDD

doi:10.5194/gmd-2015-256

NorESM-OC

J. Schwinger et al.

sink for anthropogenic CO_2, Science, 305, 367–371, doi:10.1126/science.1097403, 2004. 30, 70

Sarmiento, J. L. and Orr, J. C.: Three-dimensional simulations of the impact of southern ocean nutrient depletion on atmospheric CO_2 and ocean chemistry, Limnol. Oceanogr., 36, 1928–1950, 1991. 24

Seiter, K., Hensen, C., and Zabel, M.: Benthic carbon mineralization on a global scale, Global Biogeochem. Cyc., 19, GB1010, doi:10.1029/2004GB002225, 2005. 32, 71

Six, K. D. and Maier-Reimer, E.: Effects of plankton dynamics on seasonal carbon fluxes in an ocean general circulation model, Global Biogeochem. Cyc., 10, 559–583, 1996. 9

Smith, E.: Photosynthesis in relation to light and carbon dioxide, P. Natl. Acad. Sci. USA, 22, 504–511, 1936. 9

Steele, M., Morley, R., and Ermold, W.: PHC: A global ocean hydrography with a high-quality Arctic Ocean, J. Climate, 14, 2079–2087, 2001. 16

Takahashi, T., Broecker, W. S., and Langer, S.: Redfield ratio based on chemical data from isopycnal surfaces, J. Geophys. Res., 90, 6907–6924, 1985. 9

Takahashi, T., Sutherland, S. C., Wanninkhof, R., Sweeney, C., Feely, R. A., Chipman, D. W., Hales, B., Friederich, G., Chavez, F., Sabine, C., Watson, A., Bakker, D. C. E., Schuster, U., Metzl, N., Yoshikawa-Inoue, H., Ishii, M., Midorikawa, T., Nojiri, Y., Koertzinger, A., Steinhoff, T., Hoppema, M., Olafsson, J., Arnarson, T. S., Tilbrook, B., Johannessen, T., Olsen, A., Bellerby, R., Wong, C. S., Delille, B., Bates, N. R., and de Baar, H. J. W.: Climatological mean and decadal change in surface ocean $p\mathrm{CO}_2$, and net sea-air CO_2 flux over the global oceans, Deep-Sea Res. II, 56, 554–577, doi:10.1016/j.dsr2.2008.12.009, 2009. 29

Taylor, K. E., Stouffer, R. J., and Meehl, G. A.: An overview of CMIP5 and the experiment design, B. Am. Meteorol. Soc., 93, 485–498, doi:10.1175/BAMS-D-11-00094.1, 2012. 4

Tjiputra, J. F., Roelandt, C., Bentsen, M., Lawrence, D. M., Lorentzen, T., Schwinger, J., Seland, Ø., and Heinze, C.: Evaluation of the carbon cycle components in the Norwegian Earth System Model (NorESM), Geosci. Model Dev., 6, 301–325, doi:10.5194/gmd-6-301-2013, 2013. 3, 4, 5

Wanninkhof, R.: Relationship between wind speed and gas exchange over the ocean, J. Geophys. Res., 97, 7373–7382, 1992. 8

Warner, M. and Weiss, R.: Solubilities of chlorofluorocarbons 11 and 12 in water and seawater, Deep-Sea Res. Pt. I, 32, 1485–1497, 1985. 8

GMDD

doi:10.5194/gmd-2015-256

NorESM-OC

J. Schwinger et al.

Weiss, R.: Solubility of nitrogen, oxygen and argon in water and seawater, Deep-Sea Res., 17, 721–735, doi:10.1016/0011-7471(70)90037-9, 1970. 8

Weiss, R. and Price, B.: Nitrous oxide solubility in water and seawater, Mar. Chem., 8, 374–359, 1980. 8

5   Wolf-Gladrow, D. A., Zeebe, R. E., Klaas, C., Körtzinger, A., and Dickson, A. G.: Total alkalinity: The explicit conservative expression and its application to biogeochemical processes, Mar. Chem., 106, 287–300, doi:10.1016/j.marchem.2007.01.006, 2007. 28

GMDD

doi:10.5194/gmd-2015-256

NorESM-OC

J. Schwinger et al.

Table 1. Prognostic biogeochemical tracers in NorESM-OC.

Tracer	Abbreviation	Unit
Carbonate system		
Dissolved inorganic carbon	DIC	$kmol\,C\,m^{-3}$
Total alkalinity	TA	$keq\,m^{-3}$
Nutrients		
Phosphate	PO_4	$kmol\,m^{-3}$
Nitrate	NO_3	$kmol\,m^{-3}$
Silicate	Si	$kmol\,m^{-3}$
Dissolved iron	dFe	$kmol\,m^{-3}$
Ecosystem state		
Phosphorus in phytoplankton	PHY	$kmol\,P\,m^{-3}$
Phosphorus in zooplankton	ZOO	$kmol\,P\,m^{-3}$
Dissolved organic carbon	DOC	$kmol\,P\,m^{-3}$
Particulate organic carbon	POC	$kmol\,P\,m^{-3}$
Particulate inorganic carbon	PIC ($CaCO_3$)	$kmol\,C\,m^{-3}$
Biogenic silica (opal)	BSi	$kmol\,S\,m^{-3}$
Number of aggregates[a,b]	NOS	cm^{-3}
Mass of dust in aggregates[a,b]	aDUST	$kg\,m^{-3}$
Mass of non-aggregated dust	fDUST	$kg\,m^{-3}$
Dissolved gases		
Oxygen	O_2	$kmol\,m^{-3}$
Nitrogen	N_2	$kmol\,m^{-3}$
Laughing gas	N_2O	$kmol\,m^{-3}$
Trichlorofluoromethane[b]	CFC−11	$kmol\,m^{-3}$
Dichlorodifluoromethane[b]	CFC−12	$kmol\,m^{-3}$
Sulfur hexafluoride[b]	SF_6	$kmol\,m^{-3}$
"Preformed" tracers[b] (model diagnostics)		
Preformed oxygen	prO_2	$kmol\,m^{-3}$
Preformed phosphate	$prPO_4$	$kmol\,m^{-3}$
Preformed alkalinity	prALK	$kmol\,m^{-3}$

[a]Only if particle aggregation (prognostic sinking speed) is activated.
[b]Available as of version NorESM-OCv1.2.

GMDD

doi:10.5194/gmd-2015-256

NorESM-OC

J. Schwinger et al.

Discussion Paper | Discussion Paper | Discussion Paper | Discussion Paper

Discussion Paper | Discussion Paper | Discussion Paper | Discussion Paper |

GMDD

doi:10.5194/gmd-2015-256

NorESM-OC

J. Schwinger et al.

Table 2. Parameter values of the ecosystem parametrisation (see Maier-Reimer et al., 2005, for details) that have been changed between model version 1 and 1.2. Parameter values in brackets have been used for the model runs with the non-standard sinking schemes (Sect. 3.5).

Parameter	Symbol	Version 1	Version 1.2	Unit
Half-saturation constant for PO_4 uptake	K_{PO_4}	1×10^{-7}	4×10^{-8}	$kmol\,P\,m^{-3}$
Zooplankton assimilation efficiency	ω_{zoo}	0.5	0.6 (0.5)	–
Fraction of grazing egested	$1 - \epsilon_{zoo}$	$1 - 0.8$	$1 - 0.8$ $(1 - 0.9)$	–
Zooplankton mortality rate	λ_{zoo}	5×10^{-6}	3×10^{-6}	$(kmol\,P\,m^{-3}\,d)^{-1}$
Zooplankton excretion rate	$\lambda_{zoo,DOC}$	0.03	0.06	d^{-1}
Detritus remineralisation rate	λ_{det}	0.02	0.025	d^{-1}
DOC remineralisation rate	λ_{DOC}	0.003	0.004	d^{-1}
Opal to phosphorus uptake ratio	$R_{Si:P}$	25	30	$mol\,Si\,mol\,P^{-1}$

Discussion Paper | Discussion Paper | Discussion Paper | Discussion Paper |

GMDD

doi:10.5194/gmd-2015-256

NorESM-OC

J. Schwinger et al.

Table 3. Parameter values adopted for the prognostic sinking speed scheme.

Parameter	Symbol	Value	Unit
Minimum particle size	l	0.002	cm
Maximum particle size	L	0.5	cm
Mass of a single cell	C_l	0.0915	nmol C
Sinking speed of single cell	w_l	1.4	$\mathrm{m\,d^{-1}}$
Exponent of diameter-velocity relation	η	0.62	–
Exponent of diameter-mass relation	ζ	1.62	–
Shear parameter	Sh	0.75	$\mathrm{d^{-1}}$
Stickiness of particles	S	0.25	–
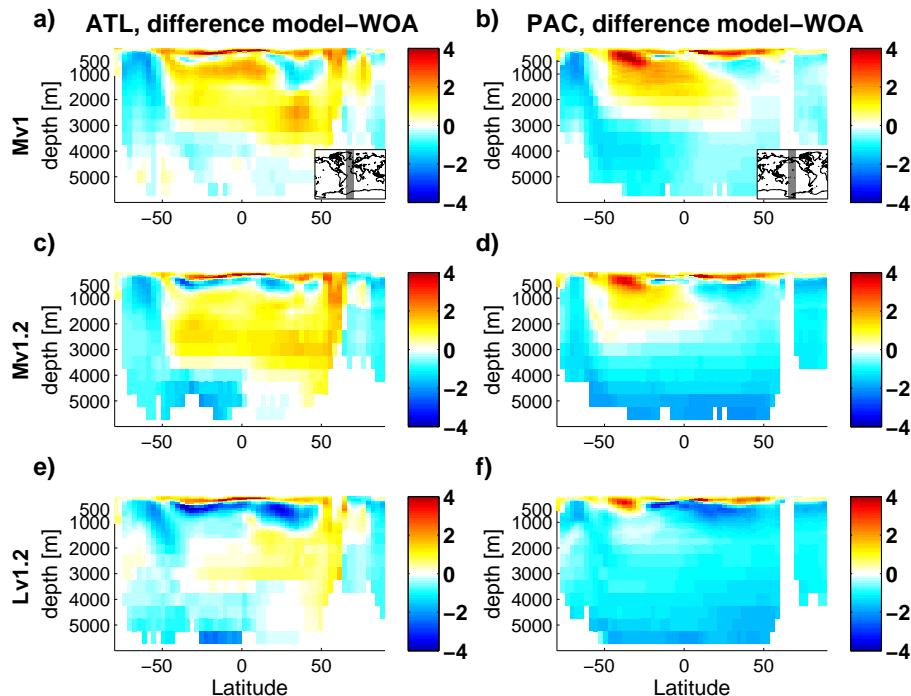
Figure 1. Temperature difference model-WOA averaged over 1965–2007 along zonal mean sections through the Atlantic/Southern Ocean **(a, c, e)** and the Pacific/Southern Ocean **(b, d, f)** for the model configurations Mv1 **(a, b)**, Mv1.2 **(c, d)**, and Lv1.2 **(e and f)**. The regions covered by the zonal mean calculations are indicated by the grey shaded area in the insets of panels **(a)** and **(b)**.

Discussion Paper | Discussion Paper | Discussion Paper | Discussion Paper

GMDD

doi:10.5194/gmd-2015-256

NorESM-OC

J. Schwinger et al.

Title Page

Abstract · Introduction

Conclusions · References

Tables · Figures

◄ · ►►

◄ · ►

Back · Close
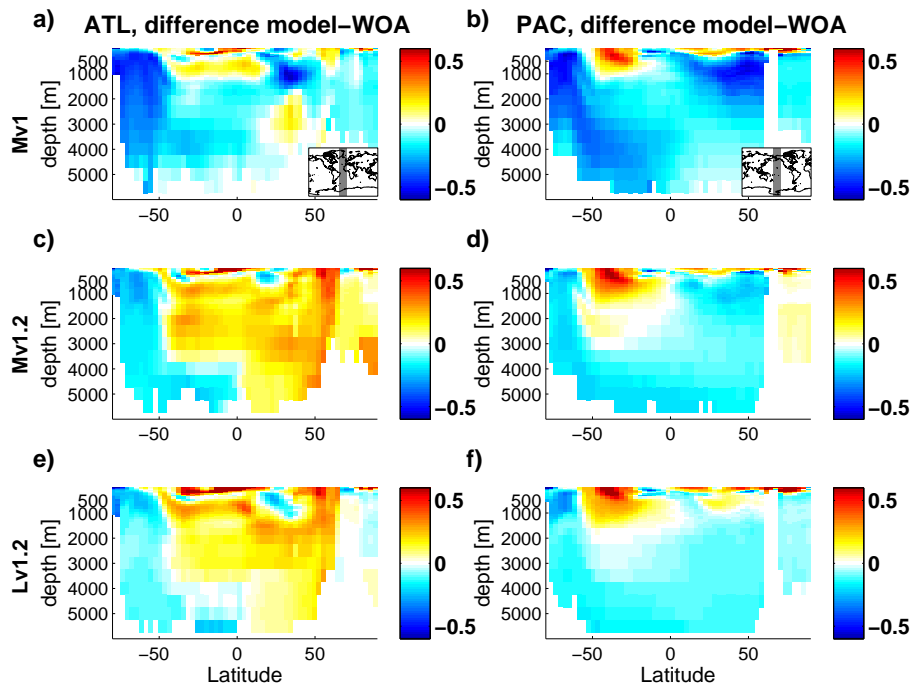
Figure 2. As Fig. 1 but for salinity.

Discussion Paper | Discussion Paper | Discussion Paper | Discussion Paper |

GMDD

doi:10.5194/gmd-2015-256

NorESM-OC

J. Schwinger et al.

Title Page

Abstract · Introduction

Conclusions · References

Tables · Figures

|◀ · ▶|

◀ · ▶

Back · Close
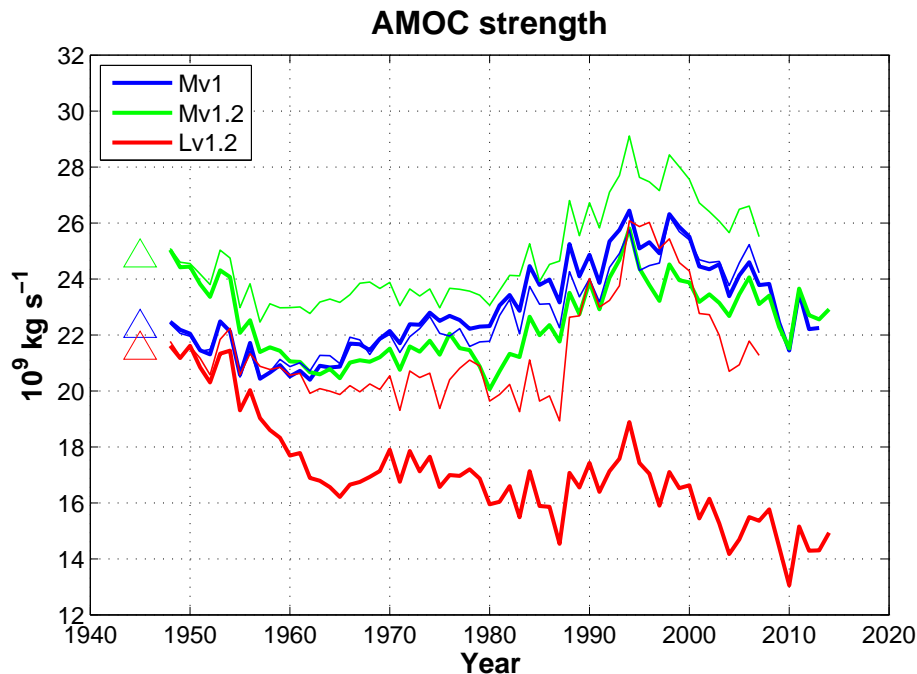
Figure 3. Atlantic Meridional Overturning Circulation measured as the maximum of the merid-ional stream-function at 26.5° N for Mv1 (blue lines), Mv1.2 (green), and Lv1.2 (red). Thick (thin) lines indicate the overturning simulated with the model forced by the NCEP-C-IAF (CORE-IAF) data set. The coloured triangles indicate the average overturning for the 30 years before switch-ing to inter-annual forcing (1918–1947).

Discussion Paper | Discussion Paper | Discussion Paper | Discussion Paper |

GMDD

doi:10.5194/gmd-2015-256

NorESM-OC

J. Schwinger et al.

GMDD

doi:10.5194/gmd-2015-256

NorESM-OC

J. Schwinger et al.
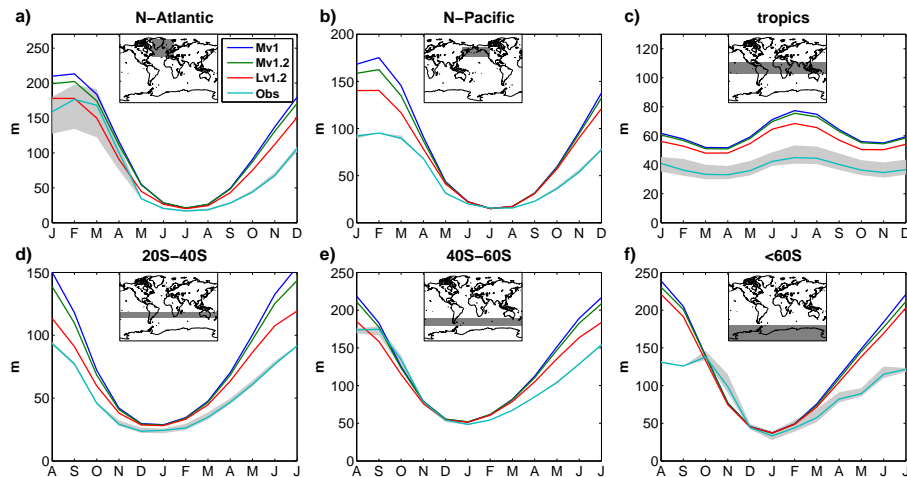
Figure 4. Mean seasonal cycle of mixed layer depth over the years 1961–2008 for **(a)** North Atlantic, **(b)** North Pacific, **(c)** tropics (20° S to 20° N), **(d)** southern subtropics (20 to 40° S), **(e)** latitudes between 40 to 60° S, and **(f)** Southern Ocean south of 60° S. Shown are results for the model configurations Mv1 (dark blue), Mv1.2 (green), and Lv1.2 (red). The light blue line and the grey shaded area give the mean and the range of the observation based climatologies of de Boyer Montégut et al. (2004). The range given for the observation based estimates is solely due to different criteria used to define MLD and not due to other uncertainties.

GMDD

doi:10.5194/gmd-2015-256

NorESM-OC

J. Schwinger et al.
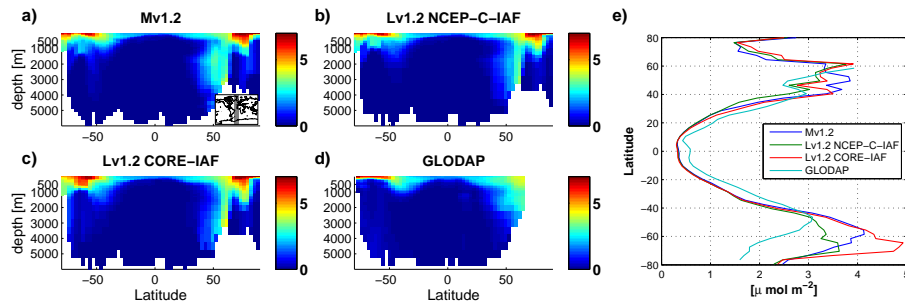
Figure 5. Zonal mean CFC-11 concentrations (nmol m^{-3}) along a section through the Atlantic/Southern Ocean (as indicated by the grey shaded area in panel **a**) averaged over the years 1988 to 1998 for the model configurations **(a)** Mv1.2, **(b)** Lv1.2 forced with NECP-C-IAF, **(c)** Lv1.2 forced with CORE-IAF, and **(d)** CFC-11 concentration taken from the GLODAP gridded data set. Panel **(e)** displays the global zonal mean CFC-11 column content (µmol m^{-2}).

GMDD

doi:10.5194/gmd-2015-256

NorESM-OC

J. Schwinger et al.
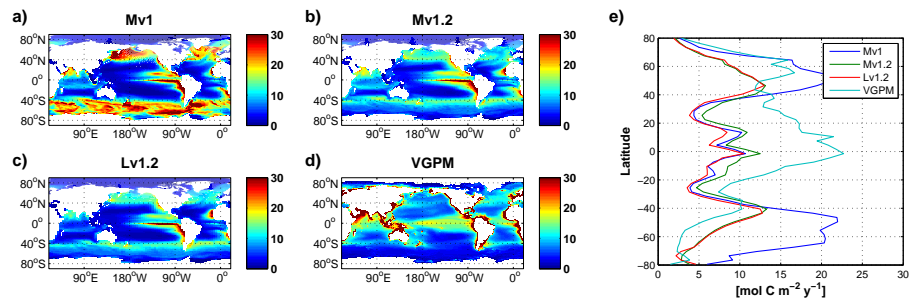
Figure 6. Vertically integrated primary production ($mol\,C\,m^{-2}\,yr^{-1}$) averaged over the years 2003–2012 for the model configurations **(a)** Mv1, **(b)** Mv1.2, **(c)** Lv1.2, and **(d)** the Eppley-VGPM satellite climatology (see text). Panel **(e)** displays the zonal means of each field presented in panels **(a–d)**.
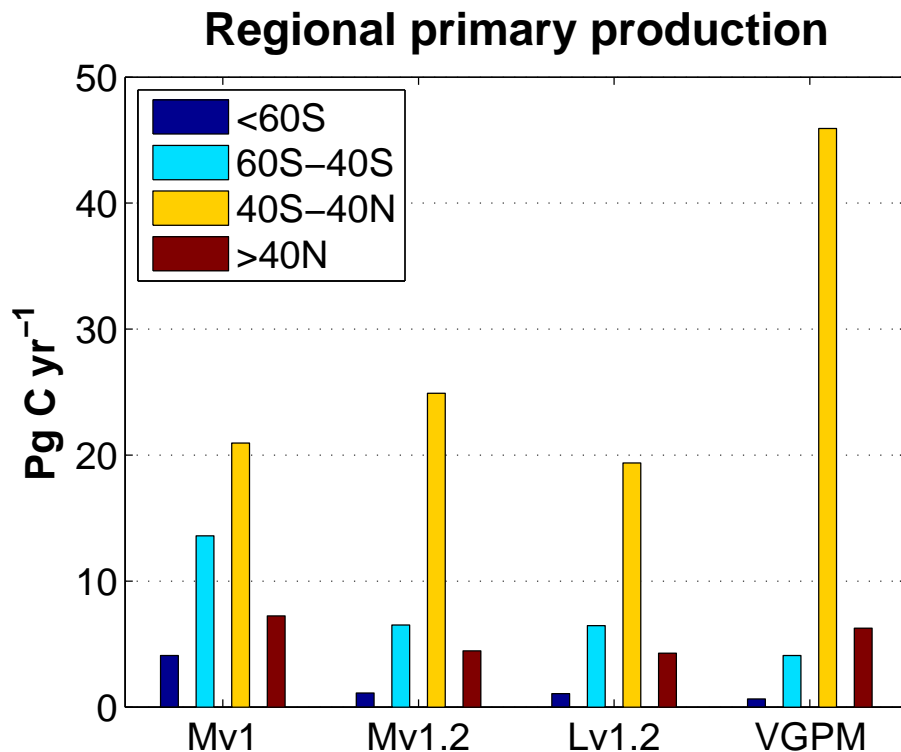
Figure 7. Mean values of total primary production over the years 2003–2012 simulated by the three different model configurations and an estimate of PP based on satellite data (VGPM, see text) for the regions indicated in the inset.

GMDD

doi:10.5194/gmd-2015-256

NorESM-OC

J. Schwinger et al.

GMDD

doi:10.5194/gmd-2015-256

NorESM-OC

J. Schwinger et al.
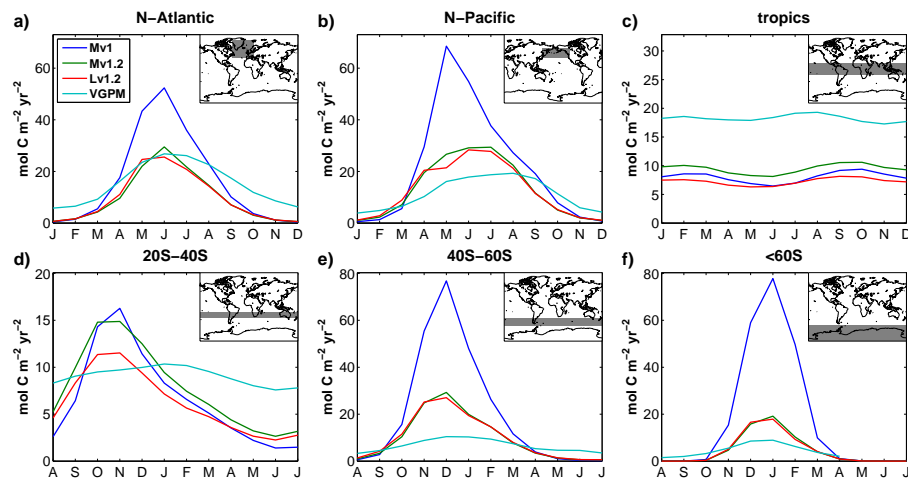
Figure 8. Mean seasonal cycle of vertically integrated primary production over the years 2003–2012 for **(a)** North Atlantic, **(b)** North Pacific, **(c)** tropics (20° S to 20° N), **(d)** southern subtropics (40 to 20° S), **(e)** latitudes between 60 to 40° S, and **(f)** Southern Ocean south of 60° S. Shown are the results for model configuration Mv1 (dark blue), Mv1.2 (green), and Lv1.2 (red) and the satellite derived seasonal cycle (light blue).
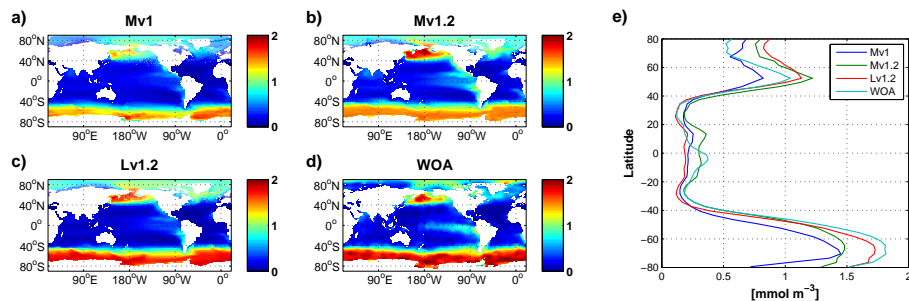
Figure 9. Surface phosphate concentration (mmol m^{-3}) averaged over the years 1965 to 2007 for the model configurations **(a)** Mv1, **(b)** Mv1.2, **(c)** Lv1.2, and **(d)** surface PO$_4$ concentration taken from the World Ocean Atlas gridded data set. Panel **(e)** displays the zonal mean of each field presented in panels **(a–d)**.

GMDD

doi:10.5194/gmd-2015-256

NorESM-OC

J. Schwinger et al.

Discussion Paper | Discussion Paper | Discussion Paper | Discussion Paper | Discussion Paper
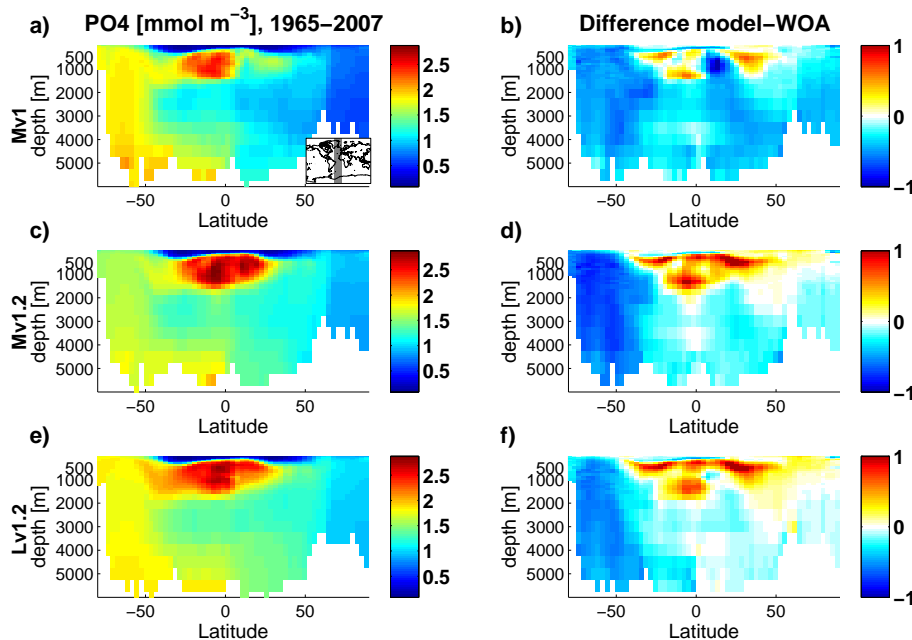
Figure 10. Zonal mean phosphate concentration (mmol m^{-3}) along the grey shaded region in the Atlantic/Southern Ocean indicated in the inset in panel **(a)** averaged over the years 1965 to 2007 for the model configurations **(a)** Mv1, **(c)** Mv1.2, and **(e)** Lv1.2. Panels **(b)**, **(d)**, and **(f)** show the differences with respect to the World Ocean Atlas gridded data set.

Discussion Paper | Discussion Paper | Discussion Paper | Discussion Paper

GMDD

doi:10.5194/gmd-2015-256

NorESM-OC

J. Schwinger et al.

Discussion Paper | Discussion Paper | Discussion Paper | Discussion Paper |

GMDD

doi:10.5194/gmd-2015-256

NorESM-OC

J. Schwinger et al.
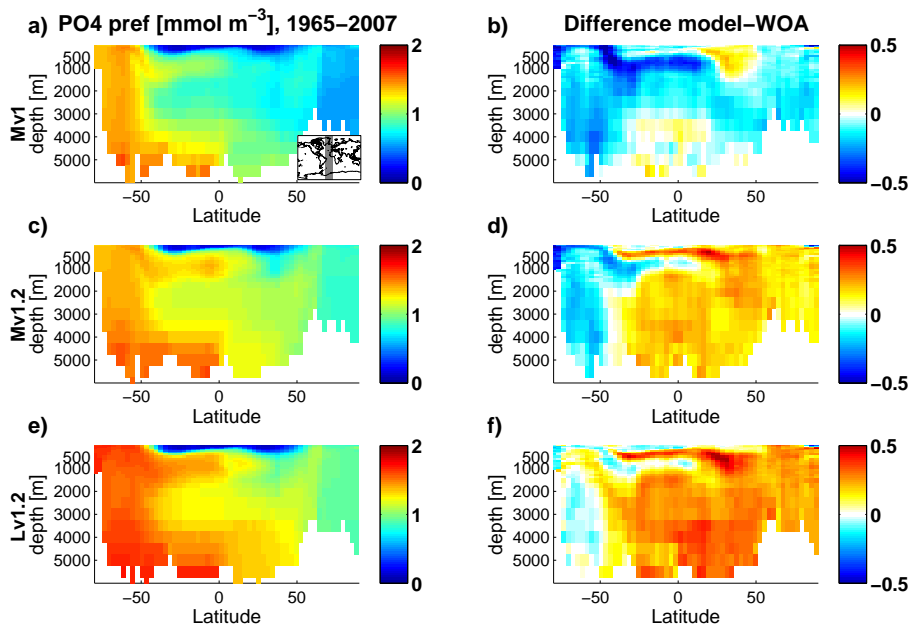
Figure 11. As Fig. 10 but for preformed phosphate (mmol m^{-3}). The remineralised fraction of phosphate is approximated by apparent oxygen utilisation (AOU) divided by the stoichiometric phosphorus to oxygen ratio $R_{O_2:P} = 172$ used in the model.

GMDD

doi:10.5194/gmd-2015-256

NorESM-OC

J. Schwinger et al.
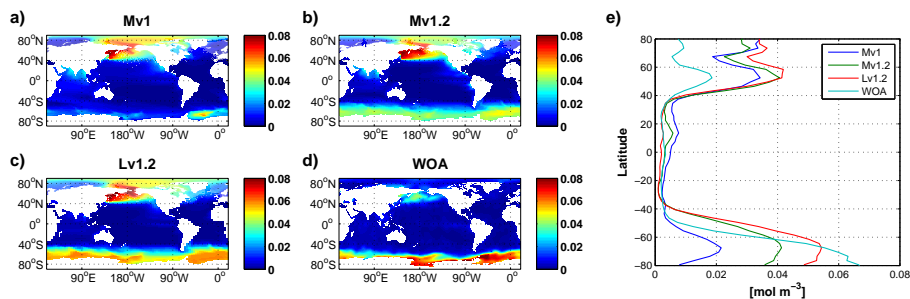
Figure 12. As Fig. 9 but for surface silicate concentrations ($\mathrm{mol\,m^{-3}}$).

GMDD

doi:10.5194/gmd-2015-256

NorESM-OC

J. Schwinger et al.
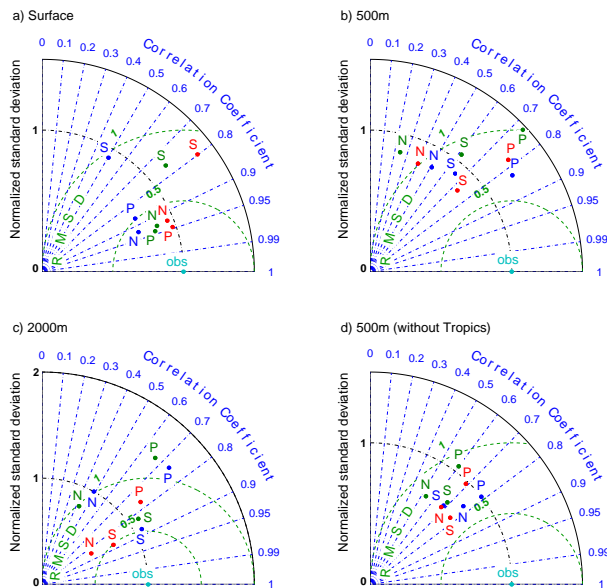
Figure 13. Taylor diagrams for phosphate (P), nitrate (N), and Silicate (S) for model configurations Mv1 (blue symbols), Mv1.2 (green), and Lv1.2 (red) at **(a)** surface, **(b)** 500 m depth, **(c)** 2000 m depth. Panel **(d)** shows results for the 500 m depth level with grid points located in the tropics (between 20° N and 20° S) omitted from the analysis. Observations are the objectively analysed climatologies from WOA 2009 (Garcia et al., 2010b). Model fields have been averaged over the time period in which the bulk of observations in WOA 2009 has been acquired (1965 to 2007).
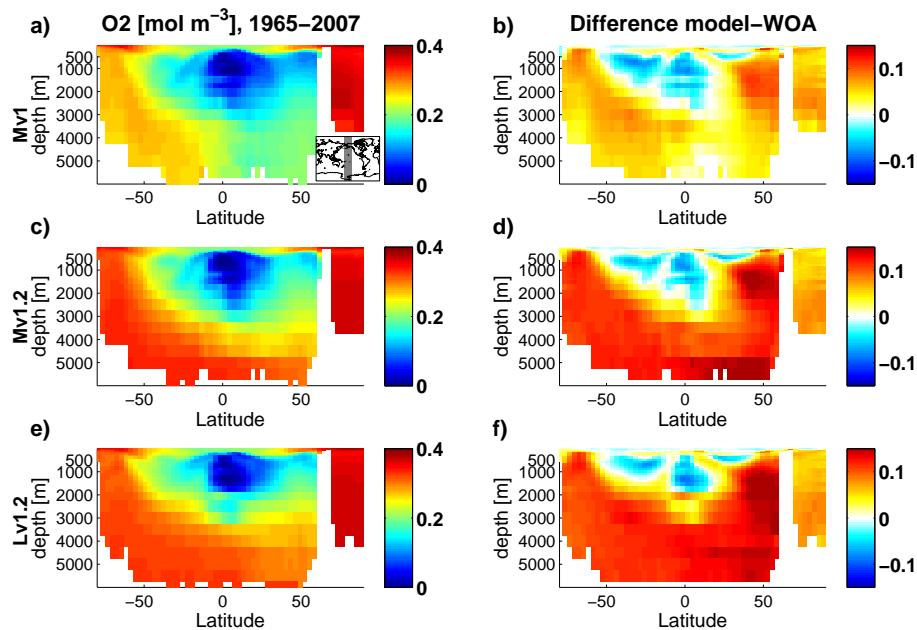
Figure 14. As Fig. 10, but for oxygen (mol m^{-3}) along the grey shaded region in the Pacific/Southern Ocean indicated in the inset in panel **(a)**.

Discussion Paper | Discussion Paper | Discussion Paper | Discussion Paper |

GMDD

doi:10.5194/gmd-2015-256

NorESM-OC

J. Schwinger et al.

GMDD

doi:10.5194/gmd-2015-256

NorESM-OC

J. Schwinger et al.
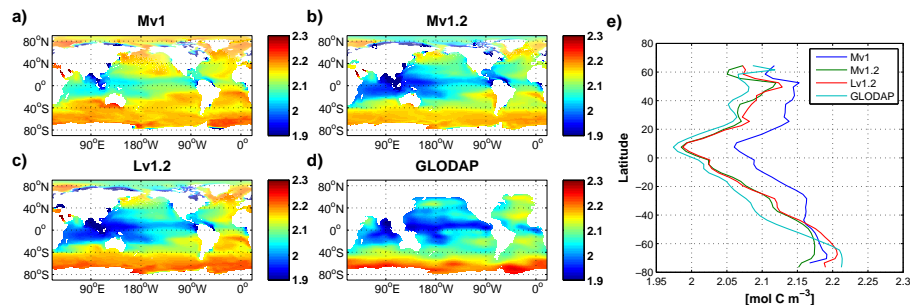
Figure 15. Surface concentration of dissolved inorganic carbon (mol m^{-3}) averaged over the years 1988 to 1998 for the model configurations **(a)** Mv1, **(b)** Mv1.2, **(c)** Lv1.2, and **(d)** corresponding surface DIC from the observation based GLODAP climatology. Panel **(e)** displays the zonal mean of each field presented in panels **(a–d)**.

Discussion Paper | Discussion Paper | Discussion Paper | Discussion Paper | Discussion Paper |

GMDD

doi:10.5194/gmd-2015-256

NorESM-OC

J. Schwinger et al.
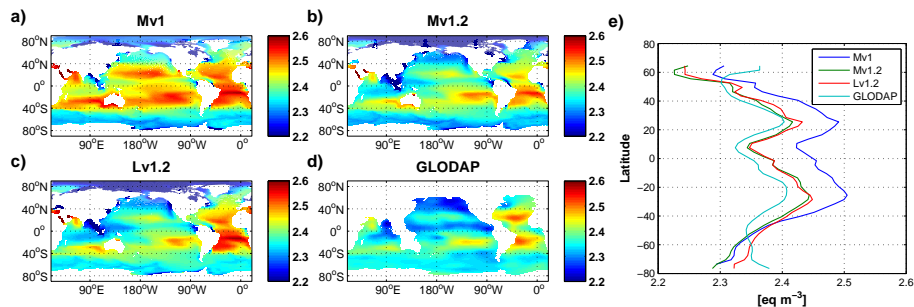
Figure 16. As Fig. 15 but for surface total alkalinity (eq m^{-3}).

Discussion Paper | Discussion Paper | Discussion Paper | Discussion Paper |

GMDD

doi:10.5194/gmd-2015-256

NorESM-OC

J. Schwinger et al.
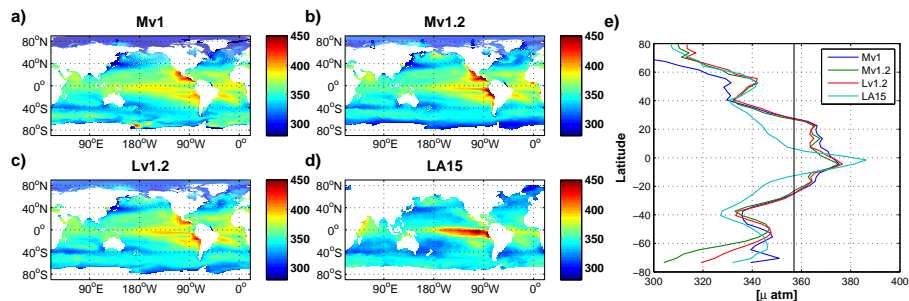
Figure 17. Surface partial pressure of CO_2 (µatm) averaged over the years 1988 to 1998 for the model configurations **(a)** Mv1, **(b)** Mv1.2, **(c)** Lv1.2, and **(d)** the observation based surface pCO_2 data set of Landschützer et al. (2015a). Panel **(e)** displays the zonal mean of each field presented in panels **(a–d)**, and the black line indicates the mean atmospheric pCO_2 over the averaging period.
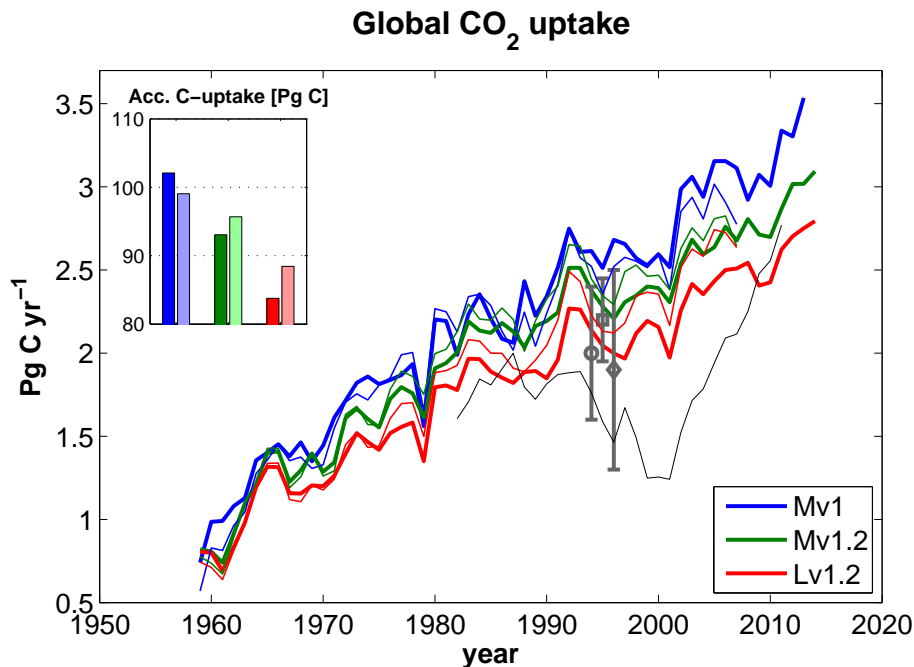
Figure 18. Globally integrated annual ocean carbon sink flux 1959–2014 for Mv1 (blue lines), Mv1.2 (green), and Lv1.2 (red). Thick (thin) lines indicate carbon fluxes simulated with the model forced by the NCEP-C-IAF (CORE-IAF) data set. The total integrated flux from 1959 to 2007 is given in the inset, where the paler shading indicates results for simulations with CORE-IAF. The thin black line is the carbon flux estimate by Landschützer et al. (2015a) assuming a constant $0.45\,\mathrm{Pg\,yr^{-1}}$ contribution of riverine outgassing flux as in Le Quéré et al. (2015). Symbols with error bars are the carbon uptake estimates by McNeil et al. (2003) (circle), Mikaloff Fletcher et al. (2006) (square), and Manning and Keeling (2006) (diamond). Note that the estimates of McNeil et al. (2003) and Manning and Keeling (2006) are mean uptake values over the 1990s.

Discussion Paper | Discussion Paper | Discussion Paper | Discussion Paper |

GMDD

doi:10.5194/gmd-2015-256

NorESM-OC

J. Schwinger et al.

Discussion Paper | Discussion Paper | Discussion Paper | Discussion Paper |

GMDD

doi:10.5194/gmd-2015-256

NorESM-OC

J. Schwinger et al.
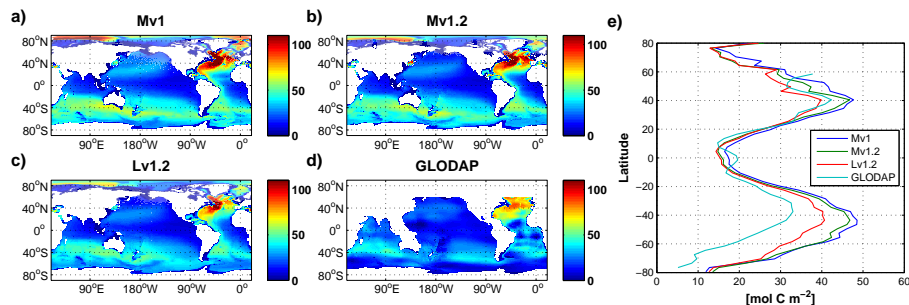
Figure 19. Vertically integrated anthropogenic carbon (mol m^{-2}) averaged over the years 1990 to 1998 for the model configurations **(a)** Mv1, **(b)** Mv1.2, **(c)** Lv1.2, and **(d)** corresponding DIC$_{ant}$ from the observation based GLODAP climatology (Sabine et al., 2004). Panel **(e)** displays the zonal mean of each field presented in panels **(a–d)**.

GMDD

doi:10.5194/gmd-2015-256

NorESM-OC

J. Schwinger et al.
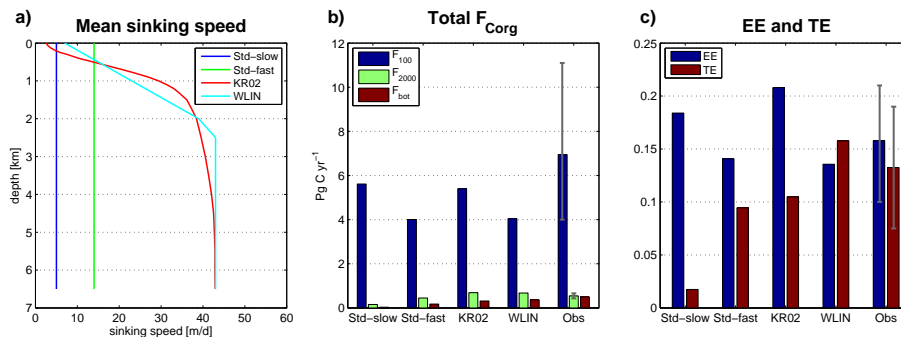
Figure 20. (a) Mean profiles of sinking speed with depth for the four experiments STD-slow (dark blue), STD-fast (green), KR02 (red), and WLIN (light blue); **(b)** globally accumulated fluxes of particulate organic carbon (POC) through 100 m depth (dark blue), through 2000 m depth (green), and the downward POC flux at the ocean bottom for depths larger than 1000 m (brown); **(c)** export efficiency (EE, dark blue) and transfer efficiency (TE, brown). The observation based estimates ("Obs") in panels **(b)** and **(c)** are derived from Henson et al. (2012), Honjo et al. (2008), and Laws et al. (2000) for POC flux at 100 m and EE, from Henson et al. (2012) and Honjo et al. (2008) for POC flux at 2000 m and TE, and from Seiter et al. (2005) for the bottom POC flux. The coloured bars indicate the mean of the observation based estimates while the grey error bars give the maximum and minimum estimate. Note that the Honjo et al. (2008) EE and TE are calculated as ratios of total PP, total export and total flux at 2000 m and not as the mean of gridded EE and TE values as the rest of the values presented here. We include these data nevertheless since the differences between the two methods of calculation are small compared to the spread of the observation based data.

Discussion Paper | Discussion Paper | Discussion Paper | Discussion Paper |

GMDD

doi:10.5194/gmd-2015-256

NorESM-OC

J. Schwinger et al.
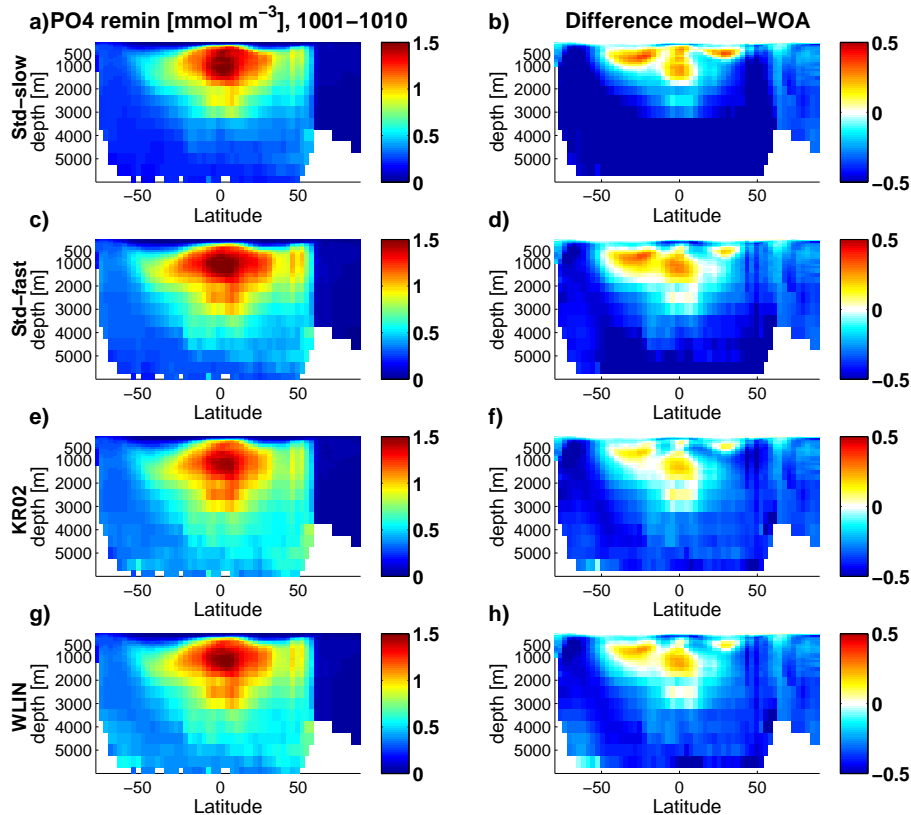
Figure 21. Global zonal mean concentrations of remineralised phosphate (mmol m^{-3}) averaged over the last 10 years of the spin-up simulations employing the **(a)** STD-slow, **(c)** STD-fast, **(e)** KR02, and **(g)** WLIN particle sinking parameterisations. Panels **(b, d, f, h)** show the differences with respect to the World Ocean Atlas gridded data set. The remineralised fraction of phosphate is approximated by apparent oxygen utilisation (AOU) divided by the stoichiometric phosphorus to oxygen ratio $R_{O_2:P} = 172$ used in the model.
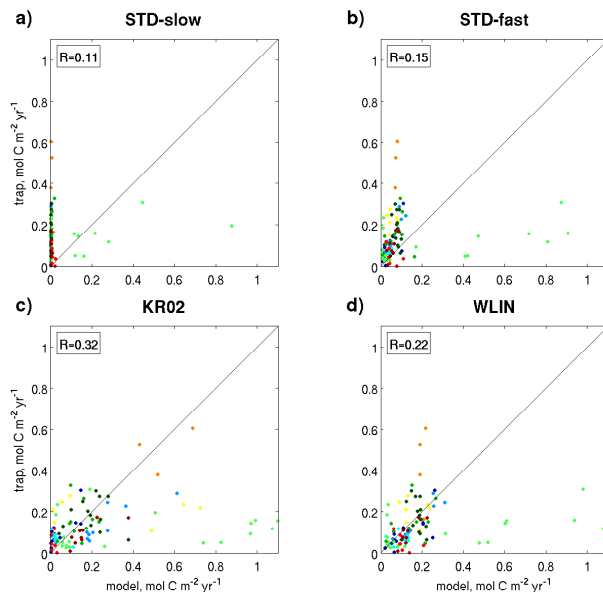
Figure 22. Scatter plots of modelled vs. observed POC fluxes at 2000 m depth for the POC sinking parameterisations **(a)** STD-slow, **(b)** STD-fast, **(c)** KR02, and **(d)** WLIN. Observed data are taken from a synthesis of sediment trap POC fluxes compiled by Honjo et al. (2008). Data from several stations are averaged if they are located in the same model grid cell. Stations are discarded if the depth in the corresponding model grid cell is shallower than 2000 m. Model-data pairs are colour coded according to ocean basin and latitudinal range: Atlantic north of 40° N (dark blue), subtropical Atlantic (blue), tropical Atlantic (light blue), Pacific north of 40° N (dark green), subtropical Pacific (green), tropical Pacific (light green), tropical Indian Ocean (yellow), Arabian Sea (orange), Southern Ocean between 40 and 60° S (brown), and Southern Ocean south of 60° S (red). Here, the term subtropical refers to latitudes between 20 and 40° N as well as 20 and 40° S, and the term tropical refers to latitudes between 20° N and 20° S.

Discussion Paper | Discussion Paper | Discussion Paper | Discussion Paper | Discussion Paper |

GMDD

doi:10.5194/gmd-2015-256

NorESM-OC

J. Schwinger et al.